Guo *et al. Biochar* (2026) 8:36
https://doi.org/10.1007/s42773-025-00552-1

Biochar

ORIGINAL RESEARCH **Open Access**

Synergistic enhancement of biochar in TiO_2/g-C_3N_4 Z-scheme heterojunction photocatalysts: mechanistic insights into the degradation pathways of sulfonamide antibiotics

Xiang Guo[1,2,4], Tong Zhou[1,3], Gongmao Wang[1], Kai Liu[1], Yu Zhang[1], Chaohai Wang[1], Junfeng Wu[1*], Biao Liu[1], Hongbin Gao[1], Xiaoxian Hu[1], Kai Jiang[2] and Dapeng Wu[2*]

Abstract

This study successfully synthesized a BC/TiO_2/g-C_3N_4 composite photocatalyst using the sol–gel method, conducted an in-depth analysis of the influence mechanism of BC on charge transfer performance in heterojunction materials, and revealed its key role in regulating the charge transport process. The introduction of biochar significantly increased the specific surface area of BC/TiO_2/g-C_3N_4 compared to the TiO_2/g-C_3N_4 catalyst, broadening the visible light absorption range. Under simulated sunlight irradiation with a wavelength greater than 420 nm, the three-component material MBC-500, calcined at 500 °C, exhibits the best catalytic performance, with an adsorption photocatalytic degradation rate of 98.13% for sulfadiazine (SDZ) within 60 min, which is 3.46, 3.40, and 2.36 times that of TiO_2, g-C_3N_4, and TiO_2/g-C_3N_4, respectively. Characterization analysis and density functional theory (DFT) calculations revealed the energy band structure and electron transfer pathways of the composite photocatalyst, indicating the significant role of biochar in electron transfer and storage. Additionally, the calculated adsorption energies demonstrated the good adsorption performance of MBC-500 for O_2 and sulfadiazine. This composite photocatalyst exhibited good stability and reusability even after five cycles of use. During the degradation process of SDZ, $\cdot O_2^-$, h^+, $\cdot OH$ play a major role.

Highlights

- BC doping boosts Z-scheme photocatalysis, increasing SDZ degradation by 2.36 times.
- DFT unveils band structure and electron transfer pathways in heterojunction.
- BC acts as an electron donor and storage medium to enhance charge transfer.

Keywords Photocatalysis, Electronic transfer, BC/TiO_2/g-C_3N_4, Z-Scheme heterojunction, Reusable, SDZ

---

*Correspondence:
Junfeng Wu
wjf8047@163.com
Dapeng Wu
dapengwu@htu.edu.cn
Full list of author information is available at the end of the article

© The Author(s) 2026. **Open Access** This article is licensed under a Creative Commons Attribution 4.0 International License, which permits use, sharing, adaptation, distribution and reproduction in any medium or format, as long as you give appropriate credit to the original author(s) and the source, provide a link to the Creative Commons licence, and indicate if changes were made. The images or other third party material in this article are included in the article's Creative Commons licence, unless indicated otherwise in a credit line to the material. If material is not included in the article's Creative Commons licence and your intended use is not permitted by statutory regulation or exceeds the permitted use, you will need to obtain permission directly from the copyright holder. To view a copy of this licence, visit http://creativecommons.org/licenses/by/4.0/.

Graphical Abstract

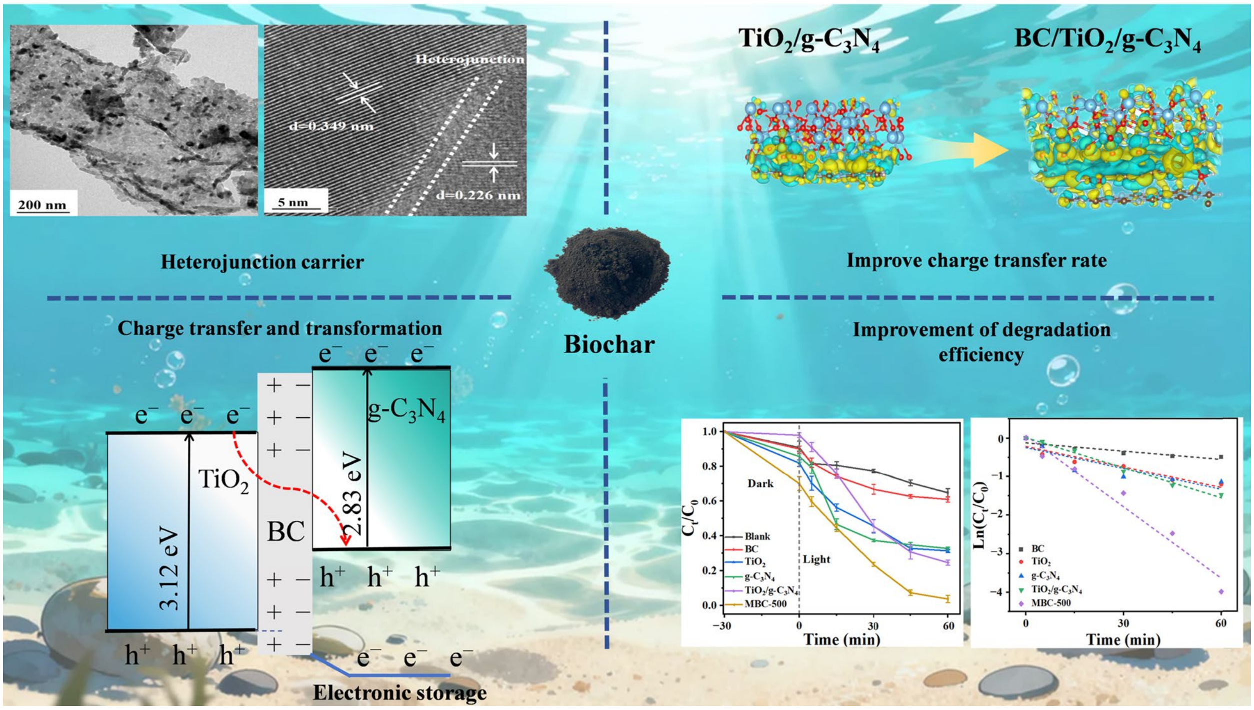

1 Introduction

The harm of antibiotic pollutants to the aquatic environment has increasingly attracted global attention. Antibiotic pollutants, particularly those represented by sulfonamides such as sulfanilamide, can alter the microbial community structure in water bodies, inhibit the growth of certain beneficial microorganisms, and thereby disrupt ecological balance. Moreover, antibiotic pollution may lead to the deterioration of water quality, compromise drinking water safety, and reduce the self-purification capacity of water bodies, further threatening human health and the sustainability of ecosystems (Li et al. 2024a, b, c, d, e; Xue et al. 2024). Therefore, effective measures are urgently needed to monitor and manage antibiotic pollutants in order to protect the aquatic environment and public health. Among various water treatment methods, advanced oxidation processes (AOPs), including photocatalysis, have attracted significant attention for the removal of antibiotic pollutants (Pan et al. 2022; Paiman et al. 2023; Zhang et al. 2023a, b, c). The development and application of new materials have become a key support in addressing complex environmental challenges—from efficient degradation of pollutants to long-term protection in extreme environments. Through precise structural design and functional regulation, new materials significantly enhance the efficiency, stability, and applicability of environmental remediation technologies (Yousefzadeh et al. 2023; Liu et al. 2025; Wang et al. 2025a, b). In the photocatalytic process, the catalysts absorb light energy to generate reactive oxygen species, which can effectively oxidize and degrade antibiotic molecules in water, thereby reducing their concentration and toxicity. Moreover, photocatalytic technology offers advantages such as ease of operation, low energy consumption, and environmental friendliness, enabling it to operate efficiently at room temperature and adapt to various water quality conditions (Long et al. 2020). As an emerging water treatment method, photocatalytic technology shows great potential in removing antibiotic pollutants.

In the realm of photocatalysis, the core of photocatalytic technology lies in the development of photocatalysts that are both efficient and stable. Semiconductor materials such as ZnO (Klienchen De Maria et al. 2024), MgO (Sharmin et al. 2021), TiO_2 (Orellana 2021), CeO_2 (Cheng et al. 2025), WO_3 (Zhou et al. 2025), CdS (Shi et al. 2020), and g-C_3N_4 (Zheng et al. 2025) are commonly used as photocatalysts. TiO_2 is a semiconductor material with broad application prospects, characterized by low cost, high catalytic activity, non-toxicity, and high stability, and it is widely used in the field of environmental remediation (Guo et al. 2019; Camacho-Munoz et al. 2020). However, the photocatalytic efficiency of pure TiO_2 is limited, mainly owing to its wide bandgap of 3.2 eV, which restricts its light absorption to the ultraviolet region, resulting in low utilization of solar energy and severe recombination of photogenerated carriers. Constructing heterojunctions is an effective strategy to address these limitations (Tan et al. 2020, 2023; Shi et al. 2024). g-C_3N_4, a metal-free photocatalyst, is valued for its abundant raw materials and excellent visible-light response, while its unique π-conjugated layered structure facilitates carrier transport (Li et al. 2024a, b, c, d, e; Wang et al. 2025a, b). Forming a TiO_2/g-C_3N_4 heterojunction can significantly broaden the light absorption range, enhance charge mobility, and reduce the recombination of photogenerated electron–hole pairs, thereby improving overall catalytic performance and reaction efficiency (Wang et al. 2019). In practical applications, enhancing the separation and migration rates of photogenerated charges in heterojunction photocatalysts is essential for achieving higher photocatalytic efficiency.

Currently, various carbon materials, such as activated carbon (Zhu et al. 2024), carbon nanotubes (Sun et al. 2019), and graphene (Bian et al. 2021), have been widely developed as semiconductor electron transport channels. The introduction of these materials has significantly improved the separation efficiency of photogenerated charges. Biochar (BC), a carbon-rich substance obtained from discarded biomass through pyrolysis, exhibits physical and chemical properties including plentiful oxygen-containing functional groups, a large surface area, and an excellent pore structure (Lu et al. 2020; Luo et al. 2023a, b). BC demonstrates notable conductivity, which can effectively reduce the recombination rate of electron–hole pairs in photocatalytic reactions, thereby enhancing the degradation rate of target compounds (Hu et al. 2025). BC is extensively utilized in the realm of photocatalysis. Abhayasimha K C et al. (K C et al. 2024) synthesized a BC/TiO_2 photocatalyst using lignin as a carbon source and ultrasound assisted co precipitation method for the removal of dye BB41, achieving a removal rate of 96.72% under their optimal experimental conditions. Wei et al. (2024) prepared a Bi_2MoO_6/porous banana peel biochar composite material using hydrothermal method. The Ciprofloxacin (CIP) degradation efficiency reached 93.6%, surpassing the previous rate by a factor of 12.2 compared to the removal efficiency obtained with the pure Bi_2MoO_6 catalyst. Luo et al. (2023a, b) prepared $Bi_2O_2CO_3$/biochar nanocomposites using a chemical co-precipitation method. The comprehensive removal rate of Tetracycline (TC) by adsorption and photodegradation within 60 min reached 84.7%, 1.5 times greater than the performance of the pure $Bi_2O_2CO_3$ photocatalyst. However, although the aforementioned studies have demonstrated the potential of BC in enhancing the performance of single or binary composite photocatalysts, research on the role and mechanism of BC in more complex heterojunction systems such as TiO_2/g-C_3N_4 heterojunctions is still in its early stages. A review of recent literature on BC-based photocatalysis reveals that most existing studies have focused on the enhancement of pollutant adsorption by BC or its role as a support for single semiconductors (Kahkeci & Gamal El-Din 2023; Zahid et al. 2025), while systematic investigations elucidating how BC acts as an electron transport bridge to regulate the band structure, interfacial charge dynamics, and ultimate reaction mechanisms of heterojunctions remain scarce. In particular, the potential influence of BC incorporation on the charge migration pathway in Z-scheme TiO_2/g-C_3N_4 heterojunctions has yet to be thoroughly explored.

In this study, BC/TiO_2/g-C_3N_4 composites were prepared with corncobs, urea, and tetrabutyl titanate as raw materials through the sol–gel method (Wang et al. 2018). The synthesized materials underwent characterization to analyze their morphology, structure, and chemical composition. Sulfadiazine served as a representative contaminant to evaluate the photocatalytic efficiency of the composite materials, and the degradation pathway of SDZ was explored. The crucial function of BC in facilitating electron transfer and storage during the photocatalytic process of heterojunction materials was elucidated through DFT. This research offers fresh perspectives on synthesizing composite photocatalysts and their use in eliminating organic pollutants.

2 Experimental section

2.1 Materials & reagents

Tetrabutyl titanate ($C_{16}H_{36}O_4Ti$), absolute ethanol (C_2H_6O), glacetic acid (CH_3COOH), nitric acid (HNO_3), and urea ($CO\ (NH_2)_2$) were acquired from the Shanghai-based China National Pharmaceutical Group Chemical Reagent Co., Ltd. Sulfadiazine (SDZ, $C_{10}H_{10}N_4O_2S$), isopropanol (IPA, C_3H_8O), triethanolamine (TEA, $C_6H_{15}NO_3$), ethylenediamine tetraacetic acid (EDTA, $C_{10}H_{16}N_2O_8$), and L-ascorbic acid (L-AA,$C_6H_8O_6$) were also obtained from the Shanghai-based China National Pharmaceutical Group Chemical Reagent Co., Ltd. Corn cobs were sourced from Pingdingshan, Henan. Throughout the study, deionized water was utilized. All other chemicals and experimental reagents were of analytical grade and used without additional purification.

2.2 Material preparation

The preparation methods of BC, TiO_2, TiO_2/g-C_3N_4, and BC/TiO_2/g-C_3N_4 can be found in the supporting material Text S1.

2.3 Analysis methods

The photocatalyst's characteristics were assessed and examined through a range of characterization techniques. Additional information is provided in Text S3.

2.4 Photocatalytic activity measurement

The effectiveness of BC/TiO_2/g-C_3N_4 in degrading SDZ was investigated under solar irradiation ($\lambda > 420$ nm). To provide a comparative analysis, the performance of BC, TiO_2, g-C_3N_4, TiO_2/g-C_3N_4, and MBC-300 (– 800) was also examined under the same experimental setup. For specific experimental operation details, please refer to Supplementary Material Text S2. The efficiencies of photodegradation for each material are presented in the following Eq. (1):

$$\text{Degradation rate (\%)} = (C_0 - C_t)/C_0 \times 100\% \quad (1)$$

In this context, the initial pollutant concentration C_0 is expressed in milligrams per liter (mg/L), while C_t represents the pollutant concentration at time t, also in mg/L.

The degradation kinetics of the pollutant using the evaluated photocatalyst adheres to a pseudo-first-order kinetic model (Miri et al. 2024), as shown in Eq. (2):

$$ln(C_0/C_t) = kt \quad (2)$$

In this equation, C_0 represents the initial concentration of the pollutant at $t=0$ (mg/L), while C_t indicates the concentration of the pollutant remaining after an irradiation period of time t (mg/L). The apparent reaction rate constant, denoted as k (min^{-1}), is calculated by analyzing the slope of the linear regression line.

3 Results and discussion

3.1 Characterization of catalysts

3.1.1 Structure and morphology

The structural and morphological characteristics of the synthesized products were analyzed using scanning electron microscopy (SEM) and high-resolution transmission electron microscopy (HRTEM). Detailed SEM and TEM characterizations of TiO_2, g-C_3N_4, and TiO_2/g-C_3N_4 are provided in the Supporting Information Fig. S1 for comparative analysis. Briefly, the sol–gel synthesized TiO_2 consists of relatively uniform particles with a size distribution of approximately 40 nm (Fig. S1a and b). The calcined g-C_3N_4 exhibits a typical 2D layered structure with distinct lamellar features clearly observable in both SEM and TEM images (Fig. S1c and d). For the sol–gel prepared TiO_2/g-C_3N_4 composite, SEM and TEM images reveal that the lamellar g-C_3N_4 surface is decorated with TiO_2 particles, resulting in a less smooth appearance compared to pure g-C_3N_4 and confirming the in situ growth of TiO_2 particles on the g-C_3N_4 surface (Fig. S1e and f).

As shown in Fig. 1a BC exhibits a rich microporous layered structure. The SEM image of MBC-500 (Fig. 1b) shows a rough surface, with the microporous structure on the BC surface covered by some layered structures and granular aggregates. Based on the morphological characteristics of TiO_2/g-C_3N_4 composite materials observed in Fig. S1e and f, it is inferred that these layered structures and granular aggregates correspond to g-C_3N_4 and TiO_2, respectively (Zhou et al. 2017). EDS analysis of MBC-500 (Fig. 1c and Fig. S2) confirms the presence of carbon (C), nitrogen (N), oxygen (O), and titanium (Ti) as the primary components, with no other elemental impurities detected. The strong Ti signal further corroborates the in situ formation of TiO_2 on the composite surface during calcination, preliminarily confirming the successful synthesis of the ternary composite.

HRTEM characterization reveals that in MBC-500, all constituent components (BC, TiO_2, and g-C_3N_4) maintain intimate interfacial contact, with the layered features of BC and g-C_3N_4 and granular morphology of TiO_2 distinctly observable on the material surface. This contrasts with the TiO_2/g-C_3N_4 binary composite, where interfacial contacts appear less uniform. Figure 1e shows that MBC-500 exhibits well-defined lattice fringe structures: the (002) plane of g-C_3N_4 with a lattice spacing of 0.226 nm, and the (101) plane of TiO_2 with a lattice spacing of 0.349 nm (Winayu et al. 2024). Notably, at the interface of these two semiconductors, TiO_2 and g-C_3N_4 are closely bonded, forming a heterojunction structure. This interface structure is more intimate and well-defined compared to that observed in the TiO_2/g-C_3N_4 composite, which is conducive to enhanced charge separation efficiency and photocatalytic activity, further validating the positive effect of BC introduction on optimizing the heterojunction interface structure (Li et al. 2023), The SAED image of MBC-500 (Fig. 1f) displays highly ordered hollow-centered rings, indicating the significant crystallinity of the composite, consistent with the HRTEM results.

Figure 2 shows the atomic force microscopy (AFM) characterization results of the TiO_2/g-C_3N_4 binary composite and the BC/TiO_2/g-C_3N_4 ternary composite. A comparison of the surface morphologies of the two composites reveals distinct microstructural differences. For the binary composite (Fig. 2a and b), the AFM images show a relatively uniform surface with a roughness of 225 nm. In contrast, the ternary composite (Fig. 2c and

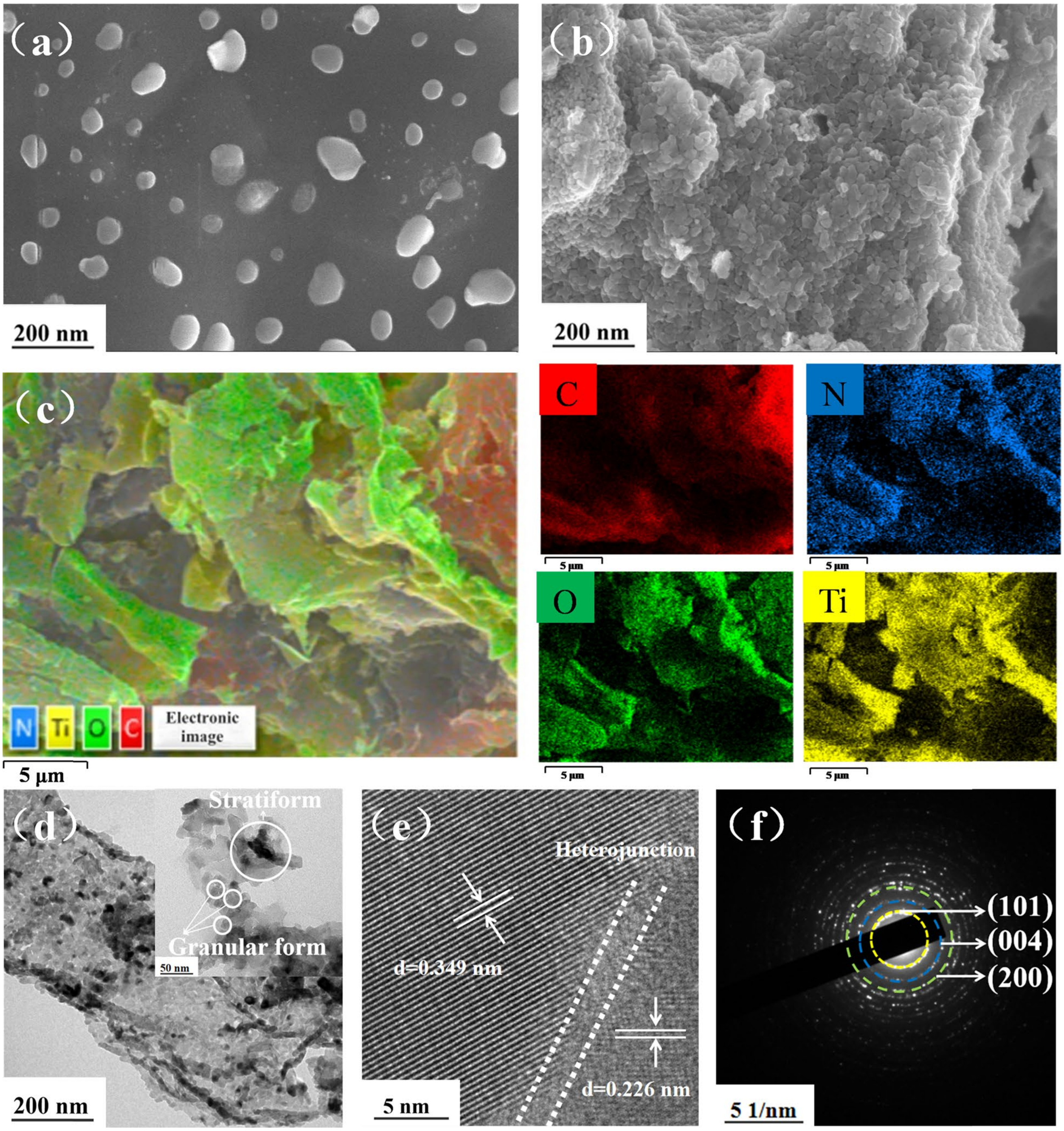

Fig. 1 (**a**) SEM image of BC; (**b**) SEM image of MBC-500; (**c**) EDS image of MBC-500; (**d**, **e**) HRTEM images of MBC-500; (**f**) SAED image of MBC-500

d) exhibits a significantly higher roughness of 444 nm. This increase in roughness may be attributed to the incorporation of biochar, whose porous and irregular structure likely contributes to the complexity of the composite's surface morphology. The introduction of biochar may promote the formation of internal pores within the material, thereby increasing the surface roughness. The higher roughness can provide more active sites, which is expected to enhance the photocatalytic efficiency.

3.1.2 Phase composition analysis

The phase composition of the synthesized photocatalyst was analyzed through X-ray diffraction (XRD) over a scanning range from 5° to 90°, as depicted in Fig. 3a. BC exhibits a broad characteristic peak at 23.73°, which

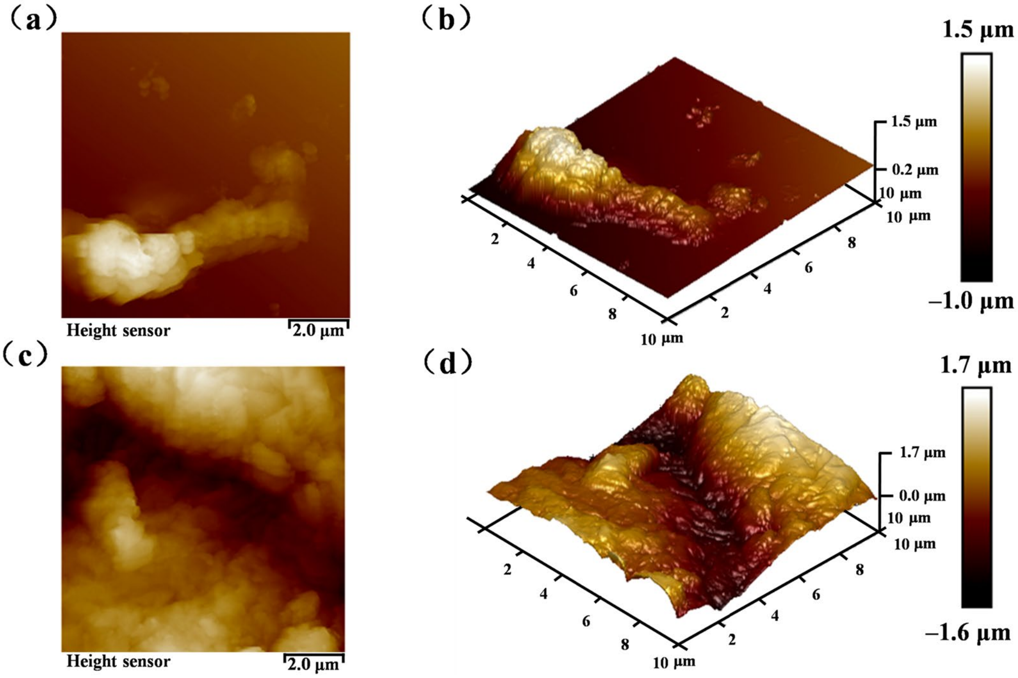

Fig. 2 AFM images of the synthesized nanoparticles: (**a**) 2D and (**b**) 3D topography of TiO_2/g-C_3N_4; (**c**) 2D and (**d**) 3D topography of MBC-500

corresponds to the (002) crystal plane of graphitic carbon. This indicates that the carbon material is partially graphitized and possesses a certain degree of crystallinity (Afzal et al. 2022). The diffraction peaks observed at 12.96° and 27.46° can be attributed to the (100) and (002) crystal planes of g-C_3N_4, respectively (Amiri & Anbia 2023). The peaks detected at 2θ angles of 25.2°, 37.8°, 48.0°, 53.8°, 55.6°, and 62.7° correspond to the (101), (004), (200), (105), (211), and (204) crystal planes of TiO_2, respectively (Beizavi & Boroujerdnia 2024). These findings suggest that in the TiO_2 doped with BC and g-C_3N_4, the anatase phase of TiO_2 is maintained; this suggests that the incorporation of g-C_3N_4 and BC does not affect the crystalline phase. The MBC-500 exhibits narrow and intense peaks, yet the diffraction peak corresponding to g-C_3N_4 around 27.46° in the composite is not prominent, which may be attributed to its low content or potential overlap with the peaks of TiO_2. The absence of extra peaks in the composite spectrum verifies that a high-purity composite has been successfully synthesized using the sol–gel technique, without any modification to the crystal structures of the individual components.

The FT-IR spectrum of the synthesized photocatalyst, illustrated in Fig. 3b, reveals several characteristic peaks. A significant peak observed at 3400 cm^{-1}, attributable to the O−H stretching vibrations, is present across all three materials (Wang et al. 2022). In the spectrum corresponding to BC, a peak at 1782 cm^{-1} is attributed to the C=O vibrations in carboxyl groups. Additionally, the peaks at 1479 cm^{-1} and 921 cm^{-1} are associated with the bending vibrations of C−H and the out-of-plane deformation of aromatic C−H, respectively (Song et al. 2020). For TiO_2/g-C_3N_4 and MBC-500, the presence of a peak at 800 cm^{-1} signifies the triazine units in g-C_3N_4. Furthermore, the range of 1200–1700 cm^{-1} displays signals characteristic of C−N heerocycles, which are indicative of g-C_3N_4 (Zeng et al. 2018). A peak observed at 495 cm^{-1} is likely due to Ti−O−Ti covalent bonds or the Ti−O stretching vibration (Wang et al. 2021).

3.1.3 Chemical state

X-ray photoelectron spectroscopy (XPS) was utilized to examine the bonding properties and chemical states of carbon (C), oxygen (O), nitrogen (N), and titanium (Ti) in MBC-500. As illustrated in Fig. 3d, the C 1s spectrum of MBC-500 is deconvoluted into two distinct peaks at 284.8 eV and 286.79 eV, which are attributed to C−C/C−Ti and C=N/C−O bonds, respectively (Rather et al. 2017). The N 1s spectrum, displayed in Fig. 3e, exhibits high resolution and predominantly features two peaks at 398.58 eV and 400.08 eV, corresponding to C=N−C and N−$(C)_3$ bonds, respectively (Wu et al. 2022). In Fig. 3f, the O 1s spectrum is resolved into two binding energy peaks located at 531.97 eV and 531.4 eV, associated with C−O−Ti and N−C−O bonds, respectively (Thi Le et al. 2024). As shown in Fig. 3g, the Ti 2p spectrum

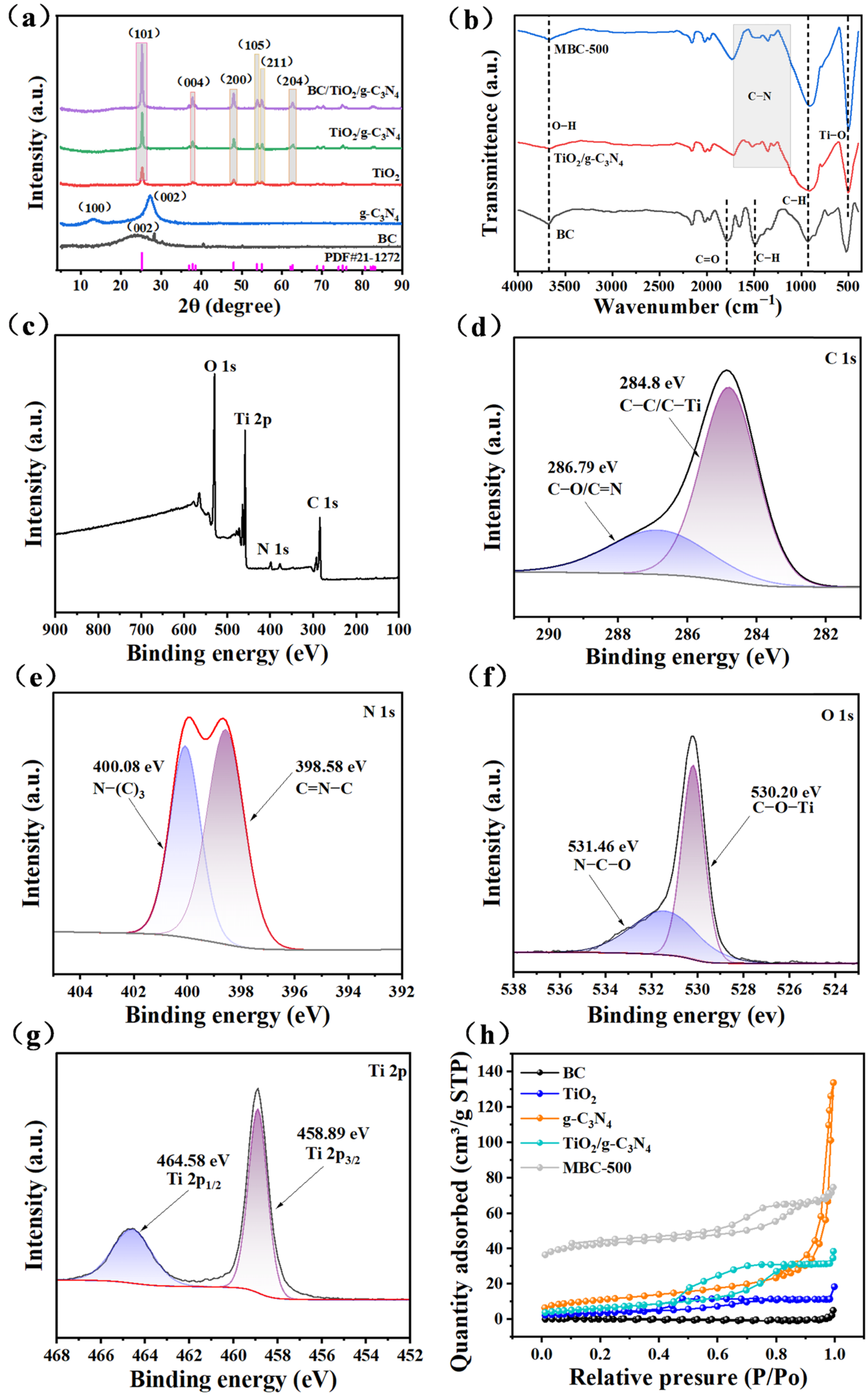

Fig. 3 (**a**) XRD spectrum; (**b**) FTIR spectroscopy; XPS spectrum of MBC-500, (**c**) Survey spectra, (**d**) C 1 s; (**e**) N 1 s; (**f**) O 1 s; (**g**) Ti 2p. (**h**) Adsorption–desorption isotherms

demonstrates two separate peaks at energies of 458.89 eV and 464.58 eV. These peaks correspond to the Ti $2p^{1/2}$ and Ti $2p^{2/3}$ orbitals, respectively, indicating distinct electronic states within the titanium material. This observation confirms that titanium in the synthesized material predominantly exists in its tetravalent oxidation state (Li et al. 2024a, b, c, d, e).

3.1.4 Specific surface area and pore size analysis

The N_2 adsorption-desorption isotherms of various materials, including BC, TiO_2, g-C_3N_4, TiO_2/g-C_3N_4, and MBC-500, are presented in Fig. 3h, showing their distinct adsorption characteristics. As indicated in Table 1, the specific surface area of BC is 0.7693 m^2/g. After loading with TiO_2 and g-C_3N_4, the specific surface area of MBC-500 increases significantly to 163.6453 m^2/g, accompanied by a reduction in pore size and an increase in pore volume. This phenomenon can be attributed to several factors. Firstly, the stacking effect of TiO_2 and g-C_3N_4 may induce substantial changes in the material's microstructure, leading to the formation of more micropores and mesopores, thereby enhancing the pore volume, as observed through high-resolution imaging of MBC-500. Secondly, the secondary calcination of BC potentially improves the pore structure by removing impurities and reinforcing the stability of the carbon framework, thereby promoting pore formation and refinement. Lastly, the inherently high specific surface area of g-C_3N_4 and its uniform dispersion in the composite significantly enhance the overall specific surface area. These synergistic effects result in optimized pore structure and a notable increase in specific surface area, which may be beneficial for the material's catalytic performance. Additionally, the synthesized material exhibits an adsorption isotherm of type IV and a hysteresis loop classified as type H_3 (Zhang et al. 2023a, b, c). This suggests that all samples feature irregular pore structures, which are characteristic of mesoporous materials. The image of MBC-500 indicates that the sample possesses a more developed microporous structure and a higher density of adsorption sites, which are conducive to enhanced catalytic performance.

Table 1 Specific surface area and pore size of prepared catalysts

Sample	BET (m^2/g)	Pore volume (cm^3/g)	Pore size (nm)
BC	0.7693	0.0078	40.6633
TiO_2	13.1172	0.0269	8.2273
g-C_3N_4	39.5073	0.2067	20.9368
TiO_2/g-C_3N_4	23.6779	0.0593	10.0281
MBC-500	163.6453	0.1152	2.8181

3.1.5 Thermal properties

This study further employed thermogravimetric analysis (TGA) to systematically investigate the weight loss behavior of the MBC-500 material at different temperature stages, providing more sufficient data support for addressing the peak overlap issue observed in XRD analysis. As show in Fig. S3, The TGA results showed that in the range of 600–800 °C, g-C_3N_4 undergoes significant mass loss, corresponding to the decomposition of carbon–nitrogen compounds into nitrogen and carbon (Bendahhou et al. 2025). For the MBC-500 sample, the approximately 20% mass loss observed between 600–700 °C can be attributed to the combined effects of the decomposition of the g-C_3N_4 component and structural changes in the biochar matrix. The high thermal stability of the biochar matrix itself, as reported in studies on similar materials (Su et al. 2024; Chaudhuri et al. 2025), suggests that the majority of this mass loss likely originates from the g-C_3N_4 phase. These data provide a basis for estimating the content of g-C_3N_4 in the composite material and further indicates its low content in the ternary composite, thereby explaining the lack of distinct characteristic peaks in the XRD pattern.

3.1.6 Optical properties

As depicted in Fig. S4, the positive slopes of the Mott-Schottky plots confirm the n-type semiconductor nature of all photocatalysts.

The photocurrent response measurements (Fig. S5a) reveal the charge separation efficiency of the photocatalysts. The photocurrent density of a material directly reflects its photogenerated charge separation efficiency; a stronger photocurrent indicates more effective charge separation (Li et al. 2024a, b, c, d, e). The TiO_2/g-C_3N_4 heterojunction exhibits a significantly enhanced photocurrent density compared to pure TiO_2, indicating that the heterojunction interface effectively facilitates the separation of photogenerated electron–hole pairs (Zhang et al. 2022). This response is further strengthened in the MBC-500 composite, suggesting that the incorporated BC acts as an electron acceptor, thereby further suppressing charge recombination and improving electron transport.

The electrochemical impedance spectroscopy (EIS) results are presented as Nyquist plots in Fig. S5b. The arc radius, which corresponds to the interfacial charge transfer resistance, follows the order of $TiO_2 > TiO_2/g\text{-}C_3N_4 >$ MBC-500. This trend confirms that MBC-500 possesses the smallest charge transfer resistance, enabling the most efficient interfacial charge transfer (Li et al. 2024a, b, c, d, e). This finding is consistent with the photocurrent response analysis shown in Fig. S5a.

In this study, UV–visible spectroscopy was utilized to examine the light absorption properties of TiO_2, g-C_3N_4, TiO_2/g-C_3N_4, and MBC-500. As illustrated in Fig. 4a, TiO_2 exhibits a distinct absorption edge near 400 nm, confirming that its excitation is confined predominantly to ultraviolet light, which inherently limits its efficiency in photocatalytic applications. In contrast, g-C_3N_4 shows an absorption edge around 460 nm, signifying its strong response to visible light. When TiO_2 is incorporated into g-C_3N_4, the resulting TiO_2/g-C_3N_4 composite exhibits a noticeable red shift in its absorption edge. This alteration indicates an expansion in the visible light absorption range, further supporting the effective formation of a heterojunction between TiO_2 and g-C_3N_4 (Miri et al. 2024). The addition of BC further amplifies this effect, as evidenced by a more pronounced red shift in the absorption edge of MBC-500. This enhancement suggests that BC significantly improves the photocatalyst's ability to harvest visible light. The inherent black coloration of BC likely contributes to its strong visible light absorption, while its incorporation may also modify the electronic structure of the composite, thereby improving photocatalytic performance (Fazal et al. 2020). The bandgap energies, calculated using the Kubelka–Munk function, are shown in Fig. 4b. The bandgap values for TiO_2, g-C_3N_4, TiO_2/g-C_3N_4, and MBC-500 are 3.12 eV, 2.83 eV, 2.56 eV, and 2.39 eV, respectively. The red shift phenomenon can be quantified by the change in bandgap values: the bandgap of TiO_2/g-C_3N_4 (2.56 eV) is reduced by 0.56 eV compared to TiO_2, while MBC-500 (2.39 eV) shows a more significant reduction of 0.73 eV. This quantitative narrowing of the bandgap demonstrates the successful extension of the light-responsive range (Othman Alqahtani 2024).

3.1.7 Surface charge and stability

Zeta potential measurements were employed to analyze the stability and surface charge characteristics of the photocatalytic nanomaterials. As shown in Fig. 4c, the surface electrical properties of the samples BC, TiO_2, g-C_3N_4, TiO_2/g-C_3N_4, and MBC-500 are observed to be positive, negative, positive, positive, and positive, respectively. The corresponding absolute Zeta potential values are 36.7 mV, 8.42 mV, 24.7 mV, 19.8 mV, and 29.4 mV. Notably, the absolute Zeta potential of MBC-500

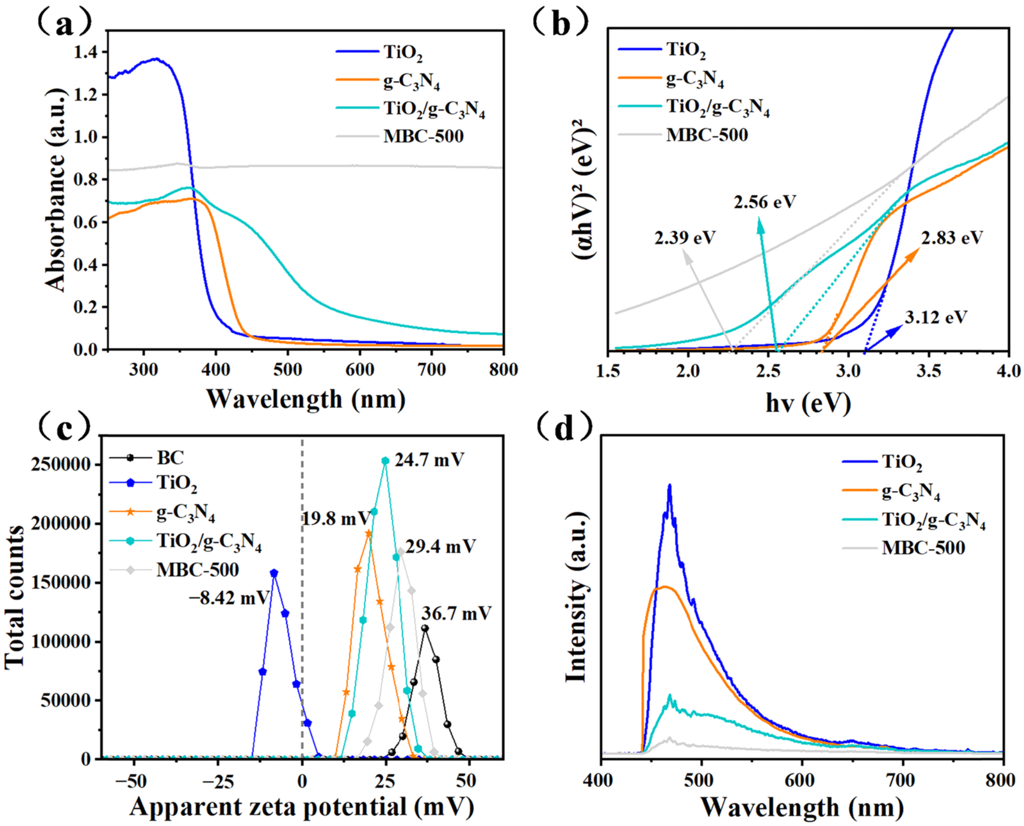

Fig. 4 (**a**) UV–Vis absorption spectrum; (**b**) A plot of $(\alpha h\nu)^2$ versus photon energy (hν); (**c**) Apparent zeta potential of the synthesized photocatalysts; (**d**) PL spectrum

is higher than that of TiO_2/g-C_3N_4, suggesting that the incorporation of biochar significantly enhances the electrostatic repulsion between particles. This increased repulsion mitigates particle aggregation, thereby ensuring superior nanoparticle dispersion. Such well-dispersed nanoparticles provide an expanded reactive surface area, thereby improving the activity and overall efficiency of the photocatalytic materials (Liu et al. 2024a, b).

Figure 4d presents the photoluminescence spectra and allows for analysis of the separation of photogenerated charge carriers in different samples. The photoluminescence spectrum provides insights into charge capture, migration, and recombination processes in semiconductor photocatalysts. A stronger PL signal correlates with higher recombination rates of photo-induced electrons and holes, suggesting reduced photocatalytic activity (Wu & Song 2023). Both pure g-C_3N_4 and TiO_2 demonstrate strong PL emission. In contrast to individual components, the TiO_2/g-C_3N_4 heterostructure shows attenuated characteristic peaks, suggesting that interfacial heterojunction formation enhances photogenerated charge migration while suppressing recombination of photo-generated charge carriers (Cui et al. 2024). When BC is incorporated, the MBC-500 composite exhibits further PL signal diminishment. This phenomenon can be attributed to two mechanisms: first, spectral overlap between PL emission and biochar absorption enables photon reabsorption (i.e., self-absorption), leading to signal reduction; second, BC plays a role in electronic storage, promoting the separation of electrons and holes (Luo et al. 2023a, b).

3.2 Photocatalytic activity

To ensure the reliability and reproducibility of all experimental results, the experimental data are the average of at least three independent parallel experiments and are presented as the mean ± standard deviation. Figure 5a shows the influence of calcination temperature on the catalyst's performance. Under irradiation at λ > 420 nm without the addition of photocatalyst, the photodegradation rate of SDZ within 90 min was 33.5%, indicating that light has a weak effect on the degradation of SDZ (Sun et al. 2020). In the dark adsorption experiment, 0.03 g of the MBC-500 catalyst was introduced into 50 mL of a 30 mg/L SDZ solution under light-shielding conditions. We conducted adsorption experiments. As shown in Fig. S6, the results demonstrate that the adsorption of SDZ onto MBC-500 reached equilibrium within 15 min. Therefore, a 30-min dark adsorption period prior to the photocatalytic experiments was sufficient to ensure the complete establishment of adsorption–desorption equilibrium in the system. The adsorption capacity of all materials under dark conditions was assessed over a period of 30 min before the photocatalytic experiment to account for the effect of direct adsorption in the analysis of photocatalytic results. As shown in the Fig. 5a, as the temperature rises, the removal rate of SDZ initially increases and then starts to decline. The catalyst calcined at 500 ℃ exhibits the best performance, achieving a removal rate of 98.13% of SDZ within 90 min. This phenomenon is closely related to the structural properties of BC, TiO_2, and g-C_3N_4 at different calcination temperatures, with the crystalline structure of TiO_2 playing a major role. At calcination temperatures below 500 ℃, TiO_2 is almost entirely composed of rutile, and rutile phase TiO_2 has good photocatalytic performance; the crystallinity of the rutile phase progressively enhances as the calcination temperature rises. With the ongoing rise in calcination temperature, the interplanar spacing and structure of TiO_2 gradually change. Above 500 °C, the microstructure of TiO_2 begins to transition from a single-phase anatase structure to rutile and brookite structures. The rutile phase begins to appear between 600 to 700 °C, while brookite phase starts to form at 800 °C (Qingge et al. 2018). Additionally,

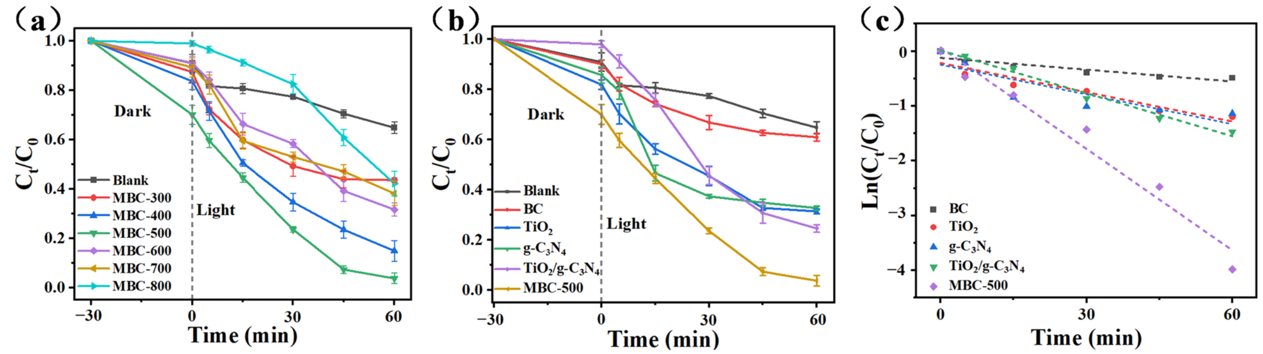

Fig. 5 (**a**) The influence of various calcination temperatures on the degradation efficiency of SDZ; (**b**) The photocatalytic performance of the synthesized samples in degrading SDZ under simulated solar irradiation (λ > 420 nm); (**c**) Kinetic curves used for the calculation of apparent rate constants

higher temperatures may enhance the stability of BC loading and improve the degradation ability of photocatalysts for SDZ, while excessively high temperatures may cause BC to undergo thermal decomposition, resulting in the loss of its structure and functional groups, thereby affecting its role in composite materials (Akca et al. 2024). At low temperatures, urea may not undergo calcination to produce g-C_3N_4. Conversely, at high temperatures, nitrogen-doped carbon is susceptible to complete gasification (Paul et al. 2019). Collectively, these factors explain the observed variation in photocatalytic performance with calcination temperature.

Figure 5b compares the performance of the ternary catalyst MBC-500 with unary and binary catalysts, clearly demonstrating its superior properties. According to BET analysis, MBC-500 demonstrates a markedly higher specific surface area and a greater density of active sites compared to BC, TiO_2, g-C_3N_4, and the TiO_2/g-C_3N_4 composite. These characteristics confer significant advantages to MBC-500 in terms of catalytic performance, thereby substantially enhancing its adsorption capacity for SDZ. Due to the positively charged nature of the SDZ surface, repulsion occurs when the photocatalyst surface is also positively charged. Among the five materials, the order of repulsive forces with SDZ molecules is MBC-500 < BC < TiO_2/g-C_3N_4 < g-C_3N_4 < TiO_2, indicating that MBC-500 experiences the weakest repulsion. This minimized repulsion allows MBC-500 to achieve a 27.57% adsorption removal rate within 30 min. Under visible light exposure for 60 min, the SDZ removal rates were 69.75% for TiO_2, 67.88% for g-C_3N_4, and 77.03% for the TiO_2/g-C_3N_4 composite. These results indicate that the heterojunction structure formed by the combination of TiO_2 and g-C_3N_4 provides a modest enhancement in photocatalytic efficiency. However, BET analysis indicates that binary composites demonstrate only slight variations in specific surface area and active sites when compared to unary materials. In contrast, the incorporation of BC into the ternary composite MBC-500 leads to a remarkable increase in specific surface area—212 times and 7 times greater than those of BC and TiO_2/g-C_3N_4, respectively. Figure 5c demonstrates that the photodegradation kinetics of SDZ by all tested materials follow a pseudo-first-order model, with MBC-500 exhibiting the highest photocatalytic rate constant at 0.0617 min^{-1}. This value is 3.46, 3.40, and 2.36 times higher than those of TiO_2, g-C_3N_4, and TiO_2/g-C_3N_4, respectively, underscoring its superior photocatalytic activity. The exceptional performance of MBC-500 is due to the synergistic interactions provided by the BC component, which optimizes the pore structure and enhances the heterojunction configuration. These enhancements considerably enhance the adsorption capacity and photocatalytic degradation efficiency of the cationic pollutant SDZ. In summary, the ternary composite MBC-500 demonstrates substantial advantages over unary and binary catalysts in terms of specific surface area, active site density, and photocatalytic efficiency. Its reduced repulsive interaction with SDZ enables rapid adsorption, while its optimized structure and enhanced heterojunction effects contribute to its exceptional photocatalytic degradation performance under visible light irradiation. These findings highlight the potential of MBC-500 for practical applications in environmental pollution control.

3.3 Stability of the photocatalyst

Cyclic tests were conducted to assess the stability and reusability of MBC-500 as an efficient photocatalyst. As depicted in Fig. 6a, after five cycles, the degradation rate of sdz by MBC-500 decreased from 98.13% to 68.85%, and after three repeated experiments, the error rate was within 1%, indicating good stability of the catalyst. In order to evaluate the stability of the catalyst and rule out the potential influence of titanium leaching, the concentration of dissolved Ti ions was measured using ICP-MS. As summarized in Table S1 and illustrated in Fig. S7, the leaching rate of Ti ions was calculated to be only 0.013%, demonstrating that the extent of titanium dissolution was very limited during the reaction. During repeated photocatalytic cycles, the porous structure of MBC-500 facilitates the adsorption and degradation of SDZ. However, recalcitrant intermediate by-products generated during the degradation process can accumulate within the catalyst's pores and on its surface. This accumulation progressively leads to pore blockage and reduced mass transfer, as the intermediates physically block the nanopores, hindering the diffusion of new SDZ molecules to the internal active sites (Mafa et al. 2023; Zhang et al. 2023a, b, c). To explore this phenomenon further, we performed SEM (Fig. 6b), FTIR (Fig. 6c), and XRD (Fig. 6d) analyses on MBC-500 after five cycles. SEM images revealed that lamellar and granular TiO_2 and g-C_3N_4 remained adhered to the BC surface, indicating no substantial morphological alterations. FTIR and XRD analyses indicated that the characteristic peaks of the catalyst remained largely unchanged after the reaction, confirming its structural stability. Therefore, the decline in catalytic performance was primarily attributed to the physical coverage of active sites and pore blockage by accumulated intermediate products.

3.4 Analysis of active species

In the photocatalytic reaction system, the potential active species include hydroxyl radicals (·OH), superoxide anions ($\cdot O_2^-$), singlet oxygen ($^1O_2$), and holes (h^+). To identify these species and assess their roles in pollutant

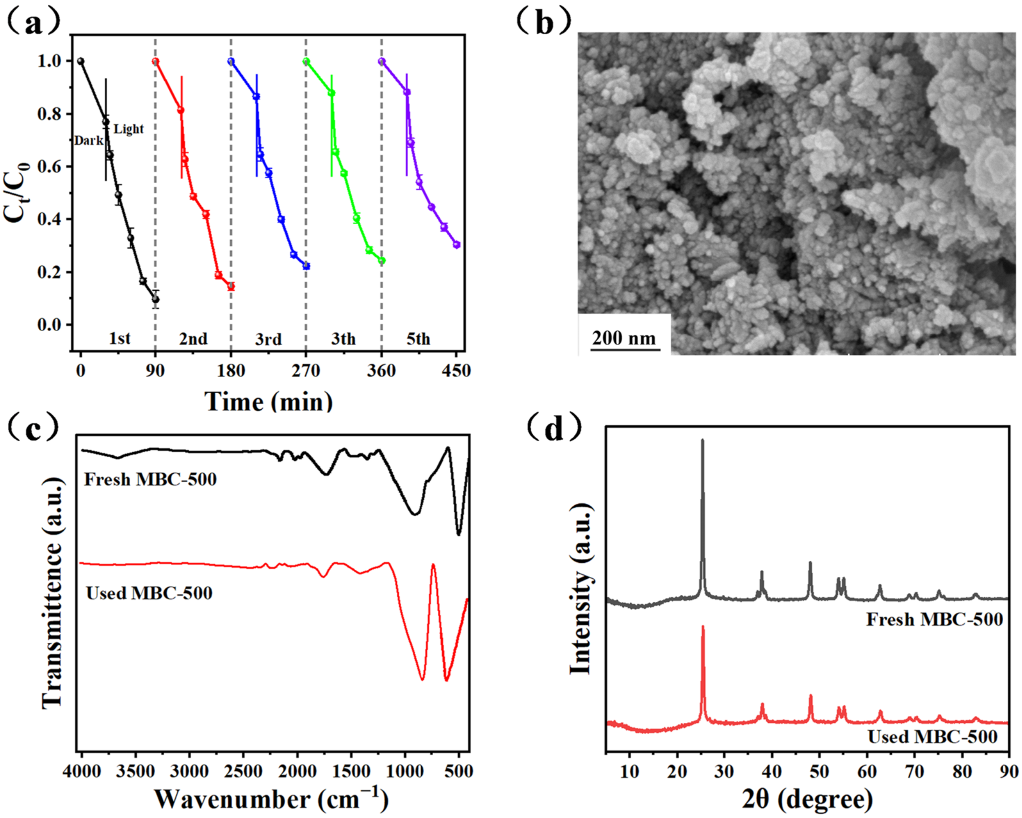

Fig. 6 (**a**) MBC-500 degrades 20 mg/L SDZ in five cycles; (**b**) Used SEM images of MBC-500; (**c**) XRD patterns of pristine and spent MBC-500; (**d**) FTIR spectra comparing the fresh and utilized MBC-500

degradation, we conducted quenching experiments and electron paramagnetic resonance (EPR) analysis. During various experimental setups, scavengers such as TEA, IPA, L-AA, and EDTA were employed to trap h^+,·OH, $^1O_2$, and·O_2^- produced throughout the degradation of SDZ (Hou et al. 2022; Kuan et al. 2022). The amount of scavengers used was 10 mmol/L (Guo et al. 2020; Liang et al. 2020). As illustrated in Fig. 7a, the SDZ degradation rate, initially at 99.13% without scavengers, decreased to 72.86%, 68.04%, 86.83%, and 65.39% with the addition of TEA, IPA, L-AA, and EDTA, respectively. This suggests that all four reactive species significantly contribute to SDZ degradation in this system. To further investigate the existence and functions of these reactive species, electron paramagnetic resonance (EPR) tests were conducted using DMPO, TEMPO, and TEMP as spin-trapping agents. Figure 7b shows that no significant signals appeared under dark conditions, but upon illumination, characteristic peaks of singlet oxygen radicals emerged, becoming more pronounced with increased exposure. Figures 7c and d reveal that while no significant DMPO-·OH and DMPO-·O_2^- signals were detected in the dark, UV irradiation led to the appearance of their characteristic peaks. The signal intensity rose with prolonged light exposure, Indicating an increase in the concentration of ·OH and ·O_2^-. Additionally, a reverse method was employed to detect h^+ (Zang et al. 2024). Peaks observed in the dark indicate captured signals, which are reduced under illumination as h^+ reacts and diminishes these signals, leading to attenuation. As depicted in Fig. S8, the spectral signal diminished significantly with longer irradiation, signifying the generation of holes. In conclusion, the photocatalytic degradation of SDZ is driven by interactions with h^+, ·OH and ·O_2^- highlighting the integral roles of these reactive species in the process.

3.5 Degradation pathways of SDZ

To uncover the mechanism behind the photocatalytic degradation of SDZ, this research employed liquid chromatography-mass spectrometry (LC–MS) to investigate the intermediates formed during the photocatalytic degradation of SDZ, while MZmine software was utilized for the screening of these intermediates. Based on the structures of the generated intermediates, Fig. 8a and Figs. S9–S16 illustrate the reaction pathway of MBC-500

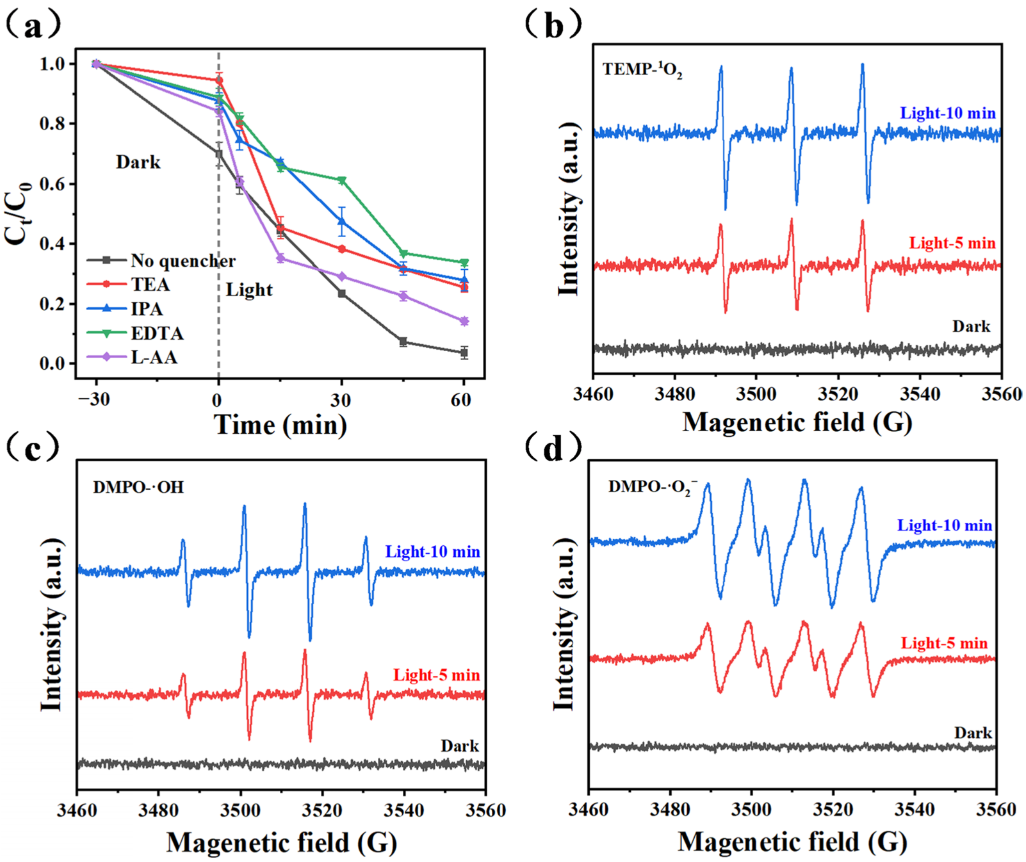

Fig. 7 (**a**) The experiments conducted to capture reactive species during the degradation of SDZ utilizing MBC-500; (**b**) EPR spectra of DMPO-$^1O_2$; (**c**) EPR spectra of DMPO-·OH; (**d**) EPR spectra of DMPO-·O_2^-

degrading SDZ under UV light irradiation. The high-resolution mass spectrometry data that form the basis for the identification of these intermediates are provided in Table S2 (Supporting Information), with the close match between experimental and calculated m/z values confirming the proposed molecular formulas.Furthermore, to gain insight into the degradation mechanism, we performed DFT calculations to estimate the reaction free energy (ΔG) for the proposed pathway of SDZ degradation. As listed in Table S3 and Fig. S19, the negative ΔG values for all elementary steps suggest that the entire pathway is thermodynamically favorable and spontaneous under the experimental conditions. This provides a thermodynamic basis for the proposed mechanism.The photocatalytic oxidation process of SDZ mainly includes four reaction processes: hydroxylation, sulfonation, oxidation, and cleavage (primarily involving the breaking of S–N and C–S bonds).

Based on the identified intermediates and the combined evidence from active species trapping experiments and Fukui function calculations, the degradation pathways of SDZ are proposed as follows (Fig. 8a).

Pathway I (·O_2^--initiated oxidation): The ·O_2^- radical, demonstrated as the most dominant active species, attacks the H–N bond of SDZ. This is consistent with the Fukui function result that the N11 atom of the aniline ring exhibits the highest f^- value (Table S4), indicating it is the most susceptible site for electrophilic attack. This reaction results in direct oxidation to produce 4-nitro-N- (pyridine-2-yl)benzenesulfonamide (P1, m/z = 281.03) (Xiang et al. 2021).

Pathway II (S–N bond cleavage): The S–N bond of SDZ is broken due to the concerted attack of ·OH and ·O_2^-, yielding 2-aminopyridine (P2, m/z = 96.06) and p-aminobenzenesulfonic acid (P3, m/z = 174.18) (Liu et al. 2018). This is supported by the fact that the S14–N17 bond is relatively long with low bond energy, making it prone to cleavage.

Pathway III (SO_2 extrusion and rearrangement): Based on the high f^+ value of the N25 atom and the significant f^- value of the C1 atom, it is inferred that the SDZ molecule undergoes SO_2 extrusion. The proposed mechanism involves nucleophilic reactions and a Smile-type rearrangement of the C and N atoms on the aniline moiety,

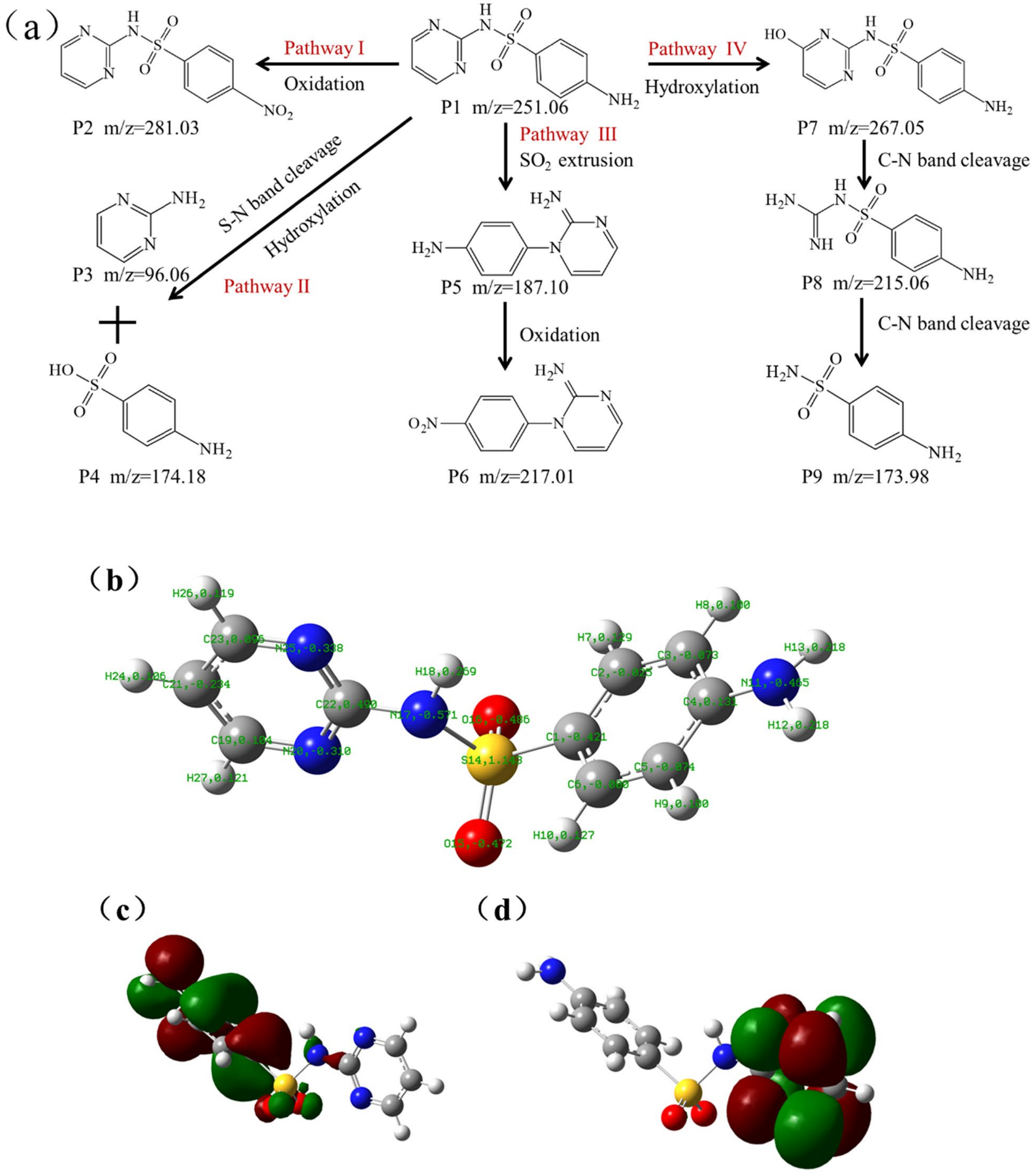

Fig. 8 (**a**) MBC-500 photocatalytic degradation pathway of SDZ; (**b**) SDZ atomic labeling optimization structure and Mulliken atomic charge; (**c**) HOMO of SDZ; (**d**) LUMO of SDZ

ultimately forming 4- (2-aminopyridine-1-yl)aniline (P5, m/z = 187.10). This is followed by the attack of $\cdot O_2^-$ on the H–N bond, producing 1- (4-nitrophenyl)−1,2-dihydropyridine (P6, m/z = 217.01) (Duan et al. 2020; Bahadoran et al. 2021).

Pathway IV (·OH-induced hydroxylation and decomposition): The hydroxyl radical (·OH) targets the carbon atom (e.g., C19 and C23 atoms with high f^0 values) located on the nitrogen-substituted benzene ring, resulting in hydroxylation and producing

4-amino-N- (4-hydroxypyridine-2-yl)benzenesulfonamide (P7, m/z = 267.05). Subsequently, the C—N bond in the heterocycle undergoes cleavage to generate 4-amino-N-[aminomethyl (aminopyridine)] benzenesulfonamide (P8, m/z = 215.06). Finally, the breaking of the C—N bond connecting to the benzene leads to the formation of 4-aminobenzenesulfonamide (P9, m/z = 173.98) (Xu et al. 2020; Chen et al. 2021; Li et al. 2025).

With the continued oxidation by reactive species, these intermediates are further mineralized into small organic molecules (CO_2 and H_2O) and inorganic ions (SO_4^{2-} and NH_4^+).

Computational modeling provides a valuable approach for elucidating the degradation pathways of SDZ and identifying potential reactive sites. The Mulliken atomic charges of the 27 atoms in the SDZ molecule were calculated, along with the distributions of the HOMO and LUMO orbitals, as shown in Fig. 8b, c, and d. The atomic natural charge and Fukui function values of SDZ and the Mulliken atomic charge data are shown in Tables S4 and S5, respectively. The results indicate that atoms such as C1, N11, N17, O15, and O16 have low electronegativity, making them susceptible to attacks from electrophilic reagents. The N11 atom exhibits the highest f^- value, confirming it as the most likely site for oxidation by $\cdot O_2^-$. The S14—N17 bond is identified as a weak point for cleavage. The high f^+ value of N25 and significant f^- value of C1 support the feasibility of the Smile-type rearrangement, while the high f^0 values of C19 and C23 atoms rationalize their susceptibility to ·OH attack, leading to hydroxylated products.

3.6 Electronic structure of BC/TiO_2/g-C_3N_4

This study investigates how BC doping influences electron transfer within the TiO_2/g-C_3N_4 heterojunction. By employing density functional theory, the study provides an in-depth analysis of the electron transfer processes and the electronic structure in the BC/TiO_2/g-C_3N_4 composite system. Initially, we calculated the density of states (DOS) for both TiO_2/g-C_3N_4 and MBC-500 composites. Figure 9a and b illustrate that the conduction band in the TiO_2/g-C_3N_4 composite predominantly arises from the N-2p, O-2p, Ti-2p, and Ti-3d orbitals, with the valence band primarily occupied by the O-2s orbital. The introduction of BC markedly modifies the electronic structure, as demonstrated by the substantial role that C-2p orbitals play in both the valence and conduction bands of MBC-500. Comparing the total DOS of TiO_2/g-C_3N_4 and MBC-500, the latter exhibits a notable increase in DOS, suggesting that BC doping substantially elevates carrier concentration, thereby enhancing photocatalytic efficiency. In addition, we determined the work function and Fermi level for these materials through our calculations. The work function, which reflects the energy needed for an electron to move from the Fermi level to the vacuum level, provides insight into the strength of electron binding. Notably, a higher work function indicates increased difficulty for electrons to escape the material. These findings demonstrate that BC doping significantly alters the electronic properties, potentially leading to improved photocatalytic performance through enhanced electron transfer capabilities (Zang et al. 2024). As shown in Figs. 9c and d, the work functions of TiO_2/g-C_3N_4 and MBC-500 are 4.53 eV and 4.73 eV, respectively, indicating that MBC-500 exhibits a stronger electron binding affinity compared to TiO_2/g-C_3N_4. This confirms that incorporating BC significantly improves the material's electron binding capacity, thereby validating BC's electron storage effect (Wei et al. 2024). Fig. S18 shows the Fermi levels of TiO_2 and g-C_3N_4.The Fermi levels of TiO_2 and g-C_3N_4 were measured to be − 4.64 eV and − 3.56 eV, respectively. As a result, electrons tend to transfer from g-C_3N_4 to TiO_2 until their Fermi levels align, leading to g-C_3N_4 becoming positively charged due to electron loss, and TiO_2 negatively charged due to electron gain, which is consistent with the zeta potential results (Meng et al. 2025). The resulting potential difference between the two materials establishes an internal electric field directed from g-C_3N_4 to TiO_2. By calculating the differential charge for both TiO_2/g-C_3N_4 and MBC-500, we analyzed electron transfer dynamics and the influence of BC in this process. As illustrated in Fig. 9e–h (with yellow and blue indicating increased and decreased charge density, respectively), in the TiO_2/g-C_3N_4 system, g-C_3N_4 loses more electrons than it gains, while TiO_2 gains more electrons than it loses, indicating net electron transfer from g-C_3N_4 to TiO_2 at their interface. With the introduction of BC, the direction of charge transfer remains unchanged; however, the magnitude of charge variation around the BC region increases significantly. This results in greater electron accumulation on TiO_2, suggesting that BC not only serves as an electron reservoir but also facilitates electron transfer. The planar charge density distribution of TiO_2/g-C_3N_4 (Fig. 9e) more intuitively illustrates a decrease in charge density on the g-C_3N_4 side and an increase on the TiO_2 side, confirming the transfer of electrons from g-C_3N_4 to TiO_2 after the formation of the heterojunction, which is consistent with the direction of the built-in electric field. Figure 9f displays the planar average charge density of MBC-500, where the charge in g-C_3N_4 and TiO_2 regions still shows a decreasing and increasing trend, respectively. The difference lies in the more pronounced change in charge density at the interface. The presence of the biochar layer significantly modulates the charge distribution between TiO_2 and g-C_3N_4, indicating that biochar acts as a bridge facilitating

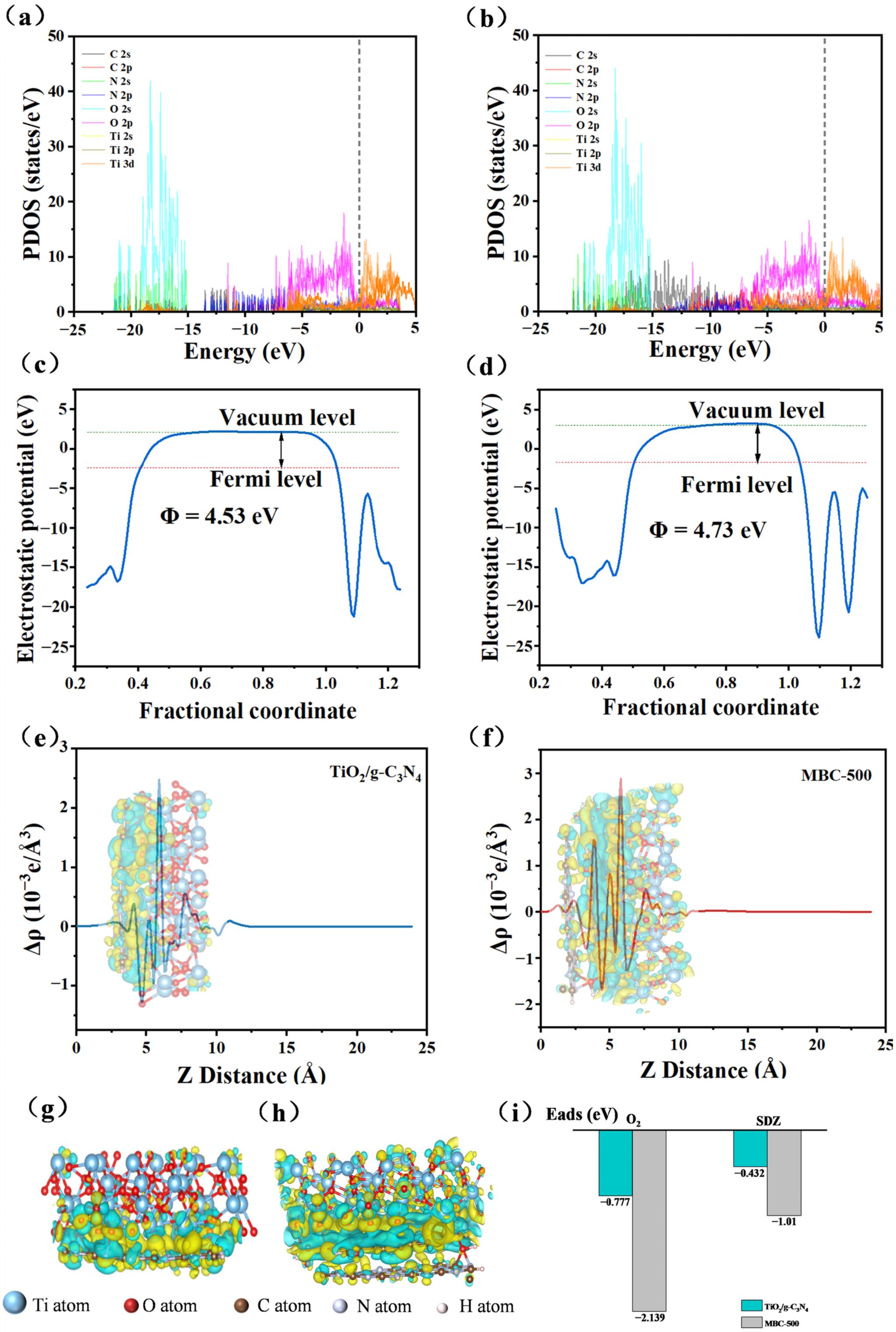

Fig. 9 (**a**) The partial density of states for TiO_2/g-C_3N_4 and (**b**) MBC-500; (**c**) The average electrostatic potential in the planar configuration of TiO_2/g-C_3N_4 and (**d**) MBC-500; (**e**, **f**) Average charge density difference of the TiO_2/g-C_3N_4 and MBC-500 heterojunctions. The inset shows the corresponding 3D isosurface of the charge density difference (**g**, **h**) show lateral perspectives of the molecular configurations along with differential charge density distributions for both TiO_2/g-C_3N_4 and MBC-500. (**i**) Adsorption energies of TiO_2/g-C_3N_4 and MBC-500 for oxygen and SDZ

electron transfer and charge redistribution. Bader charge analysis quantified the electron transfer amounts in TiO_2/g-C_3N_4 and MBC-500 to be 0.5 e^- and 0.77 e^-, respectively, further indicating that biochar enhances electron transfer (An et al. 2023). Moreover, as depicted in Fig. 9i, calculations of adsorption energies for O_2 and sulfadiazine on TiO_2/g-C_3N_4 and MBC-500 demonstrate that MBC-500 exhibits a higher propensity to adsorb these molecules, thereby accelerating surface reaction kinetics (Liu et al. 2024a, b). Upon light irradiation, TiO_2 and g-C_3N_4 generate photogenerated electrons and holes, respectively. Because the MBC-500 heterojunction has a narrower bandgap (2.39 eV) than its individual components, TiO_2 (3.12 eV) and g-C_3N_4 (2.83 eV), its enhanced light absorption capability leads to a greater yield of photogenerated charge carriers. More critically, the band alignment of the heterojunction facilitates the interfacial recombination of photogenerated electrons and holes at the TiO_2/g-C_3N_4 interface, the rate of which exceeds that of bulk recombination within each individual material. Furthermore, the built-in electric field, directed from g-C_3N_4 to TiO_2, exerts a driving force on the charge carriers and causes band bending: the energy bands bend upward in the positive space charge region on the g-C_3N_4 side, and downward in the negative space charge region on the TiO_2 side.The narrower bandgap of the MBC-500 heterojunction, combined with the built-in electric field and band bending from g-C_3N_4 to TiO_2, collectively promote the recombination of photogenerated electrons in the conduction band (CB) of TiO_2 with photogenerated holes in the valence band (VB) of g-C_3N_4. However, these effects inhibit the transfer of photogenerated electrons from the CB of g-C_3N_4 to the CB of TiO_2, as well as the transfer of photogenerated holes from the VB of TiO_2 to the VB of g-C_3N_4 (Zhu et al. 2025).

Figure 10 presents the electron localization function (ELF) analysis, where the red and blue regions correspond to the highest (ELF = 1) and lowest (ELF = 0) values, indicating localized electron accumulation and depletion, respectively (Huang et al. 2025). The ELF distribution in MBC-500 demonstrates pronounced electron sharing between BC and the TiO_2/g-C_3N_4 composite, suggesting that their interaction is predominantly covalent in nature. At the interface between BC and g-C_3N_4, carbon atoms from biochar form covalent bonds with nitrogen atoms of carbon nitride. Furthermore, since both biochar and carbon nitride contain abundant carbon atoms, π–π interactions, a type of noncovalent interaction, may also be present, enhancing the stability and electrical conductivity of the material. At the BC and TiO_2 interface, covalent bonds are formed between carbon atoms in biochar and oxygen atoms in titanium dioxide. Additionally, as both biochar and TiO_2 are nonpolar or weakly polar materials, van der Waals forces may exist between them. Although relatively weak, these interactions can still influence the physical properties of the material to some extent.

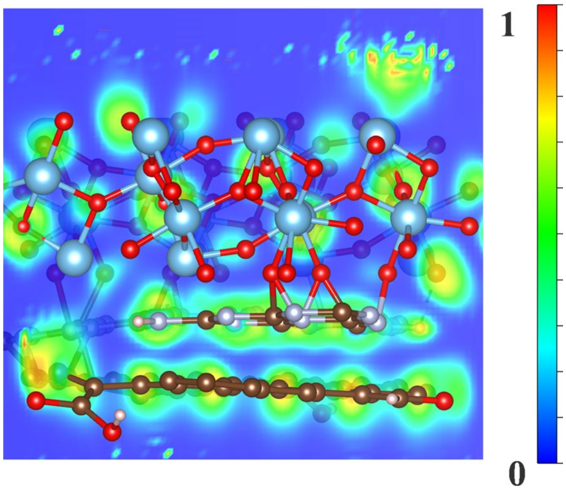

Fig. 10 ELF image of MBC-500

3.7 Photocatalytic mechanism

Building upon the aforementioned band structure analysis and DFT calculations, we propose a mechanism for the degradation of sulfadiazine by MBC-500 when exposed to simulated sunlight, as illustrated in Fig. 11. The energies of the conduction band (ECB) and the valence band (EVB) were determined by applying Eqs. (3) and (4) provided below (Klüpfel et al. 2014).

$$E_{CB} = \chi - E^0 - 1/2E_g \tag{3}$$

$$E_g = E_{VB} - E_{CB} \tag{4}$$

where, χ is the electronegativity of the semiconductor, and the values of g-C_3N_4 and TiO_2 are 4.73 and 5.81 eV, respectively (Kane et al. 2022). E_0 is the energy of free electrons relative to NHE (4.5 eV) (Lin et al. 2021). The band gap energies (Eg) obtained from the UV–visible absorption spectra in this study for TiO_2 and g-C_3N_4 are 3.12 eV and 2.83 eV, respectively. Then, the ECB and EVB were calculated, with the conduction and valence band potentials of TiO_2 being − 0.25 eV and + 2.87 eV, and those of g-C_3N_4 being − 1.19 eV and + 1.64 eV. In the case of a conventional type II heterojunction formed between TiO_2 and g-C_3N_4, electrons present in the conduction band of g-C_3N_4 tend to move to the conduction band of TiO_2. Conversely, holes in TiO_2's valence band are likely to transfer to the valence band of g-C_3N_4. Specifically, the conduction band potential

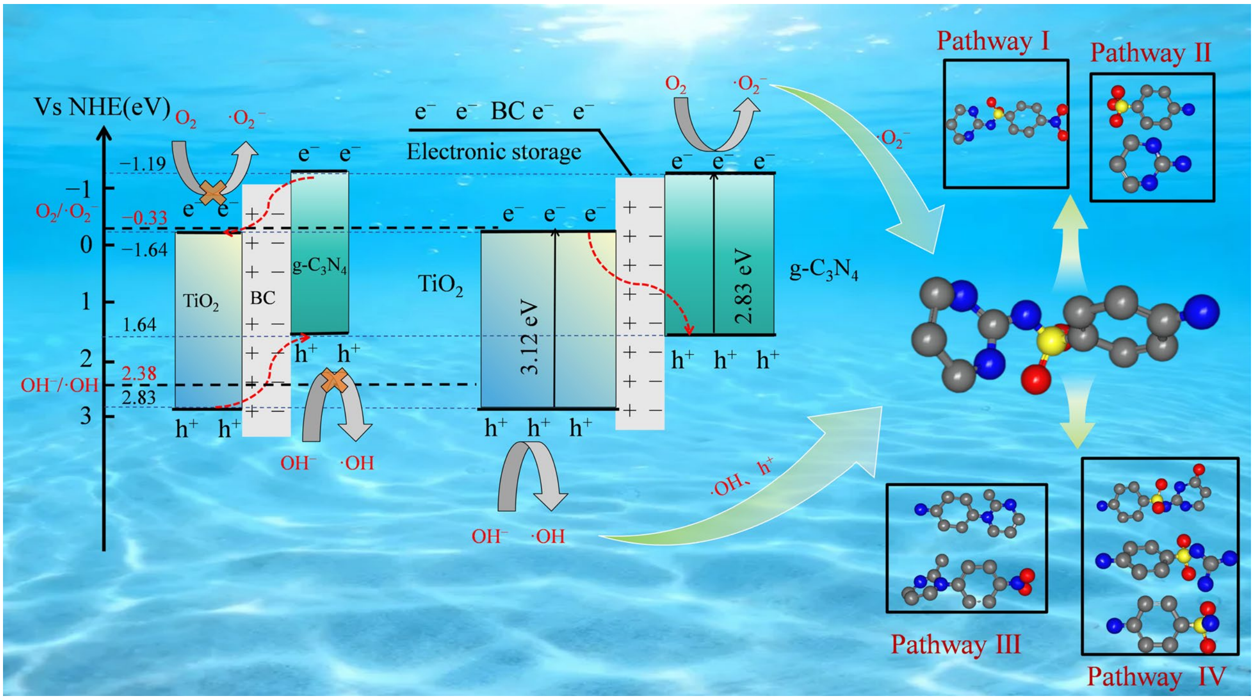

Fig. 11 The photocatalytic mechanism of MBC-500 photocatalytic system

of TiO_2 is − 0.25 eV (relative to the standard hydrogen electrode, NHE), exceeding the $O_2/\cdot O_2^-$ potential, which is more positive than the − 0.33 eV (Ma et al. 2022). Meanwhile, the valence band potential of g-C_3N_4 is 1.64 eV (relative to NHE), which is less positive than the $OH^-/\cdot OH$ potential level of 2.38 eV when referenced to the normal hydrogen electrode (NHE) (Zhang et al. 2021), indicating that holes in the g-C_3N_4 valence band are unable to oxidize OH^- to ·OH. These predictions, however, contradict the electron paramagnetic resonance results that confirmed the generation of both $\cdot O_2^-$ and ·OH radicals, suggesting that the heterojunction does not follow a typical type II mechanism. Instead, the photocatalytic performance of the sample can be interpreted using a Z-scheme heterojunction model. In this model, the light-induced electrons move from the conduction band of TiO_2 to the valence band of g-C_3N_4, where they recombine with the photo-induced holes. This process leaves a greater number of reductive electrons in the conduction band of g-C_3N_4 and more oxidative holes in the valence of TiO_2, enhancing the photocatalytic efficiency. The differentiation of electrons and holes promotes the generation of ·OH and $\cdot O_2^-$ radicals, the hole potential in the valence band of TiO_2 (+ 2.87 eV) exceeds that of the $OH^-/\cdot OH$ pair (+ 2.38 eV, referenced to NHE), and the electron potential in the conduction band of g-C_3N_4 (− 1.19 eV) is lower than that of the $O_2/\cdot O_2^-$ pair (− 0.33 eV, relative to NHE).

The primary reaction steps involved in this mechanism under light exposure are outlined in the following equations:

$$TiO_2 + h\nu = e^-(TiO_2) + h^+(TiO_2) \tag{5}$$

$$g - C_3N_4 + h\nu = e^-(g - C_3N_4) + h^+(g - C_3N_4) \tag{6}$$

$$e^-(g - C_3N_4) + O_2 = g - C_3N_4 + \cdot O_2^- \tag{7}$$

$$h^+(TiO_2) + H_2O/OH^- = TiO_2 + \cdot OH \tag{8}$$

$$h^+ + \cdot O_2^- + \cdot OH + SDZ = degradation\,products \tag{9}$$

4 Conclusion

This study thoroughly investigates the role of BC doping in enhancing the photocatalytic efficiency of Z-scheme heterojunctions. A new photocatalyst, MBC-500, was successfully prepared using the sol–gel technique. Its structure, composition, and properties were thoroughly characterized and confirmed using a suite of analytical techniques. The study revealed that the Z-scheme heterojunction formed by g-C_3N_4 and TiO_2 markedly inhibited the recombination of electron–hole pairs. This suppression leads to a more efficient separation of photogenerated charge carriers, ultimately improving the photodegradation efficiency of SDZ. BC doping played a pivotal role in this enhancement by increasing the specific surface area, expanding the visible light absorption range, and acting as an electron donor and storage center. Compared to the undoped TiO_2/g-C_3N_4 composite, MBC-500's degradation rate of SDZ improved by 2.36 times, underscoring the importance of BC doping. Active species such as h^+, $\cdot O_2^-$, and ·OH were crucial during the SDZ degradation process. Furthermore, the MBC-500 photocatalyst demonstrated remarkable stability and reusability even after five cycles of use. This study provides a photocatalytic solution for efficiently removing organic pollutants from wastewater, offering a scientific basis for optimizing heterojunction photocatalyst design and application.

Supplementary Information

The online version contains supplementary material available at https://doi.org/10.1007/s42773-025-00552-1.

Supplementary Material 1.

Acknowledgements

The authors acknowledge: Science and Technology Project of Henan Province (Grant Nos. 242102321078, Grant Nos. 242102320082, Grant Nos. 242102321044, Grant Nos.252102320067).

Author contributions

These authors contributed equally. All authors have given approval to the final version of the manuscript. Xiang Guo: Conceptualization, Project administration, writing-review & editing. Tong Zhou: Investigation, Methodology, Data curation, Writing-original draft, Writing-review & editing. Gongmao Wang, Yu Zhang and Kai Liu: Investigation, Methodology. Xiaoxian Hu, Kai Jiang, Hongbin Gao and Biao Liu: Validation, Supervision. Junfeng Wu, Chaohai Wang and Dapeng Wu: Project administration, supervision, Funding acquisition.

Funding

Henan Provincial Science and Technology Research Project, 242102320082, Xiang Guo, 242102321078, Xiaoxian Hu, 242102321044, Biao Liu, 252102320067, Hongbin Gao.

Data availability

We would like to respectfully emphasize that the experimental data, characterization results, and corresponding analyses presented throughout the manuscript and in the supporting information have been carefully curated to thoroughly substantiate the conclusions drawn in this study. We are confident that these materials provide a solid foundation for evaluating the validity and implications of our work. In the spirit of academic collaboration and transparent scientific discourse, we also wish to extend our willingness to share further underlying data that may be of interest. Should fellow researchers require access to specific raw datasets for deeper examination or additional verification, we warmly invite them to contact the corresponding author via email. We will be glad to provide the relevant materials in a timely manner to facilitate continued scholarly exchange.

Declaration

Competing interests

All authors declare that they have no competing interests relevant to the content of this article.

Author details

[1]Henan Key Laboratory of Water Pollution Control and Rehabilitation Technology, Henan International Joint Laboratory for Green Low Carbon Water Treatment Technology and Water Resources Utilization, School of Municipal and Environmental Engineering, Henan University of Urban Construction, Pingdingshan 467036, China. [2]Henan Key Laboratory for Environment Pollution Control, School of Environment, Henan Normal University, Xinxiang 453007, China. [3]School of Environmental and Municipal Engineering, North China University of Water Resources and Electric Power, Zhengzhou 450046, China. [4]Key Laboratory of Integrated Regulation and Resources Development of Shallow Lakes of Ministry of Education, Hohai University, Nanjing 210098, China.

Received: 7 May 2025 Revised: 29 October 2025 Accepted: 10 November 2025

Published online: 26 February 2026

References

Afzal MZ, Zu P, Zhang C, Guan J, Song C, Sun X, Wang S (2022) Sonocatalytic degradation of ciprofloxacin using hydrogel beads of TiO_2 incorporated biochar and chitosan. J Hazard Mater 434:128879. https://doi.org/10.1016/j.jhazmat.2022.128879

Akca MO, Bozkurt PA, Gokmen F, Akca H, Yacolu KD, Uygur V (2024) Engineering the biochar surfaces through feedstock variations and pyrolysis temperatures. Ind Crops Prod. https://doi.org/10.1016/j.indcrop.2024.118819

Amiri S, Anbia M (2023) Enhanced degradation of diazinon in aqueous solution using C-TiO_2/g-C_3N_4 nanocomposite under visible light: synthesis, characterization, kinetics, and mechanism studies. Mater Res Bull 165:112289. https://doi.org/10.1016/j.materresbull.2023.112289

An X, Xu X, Guo W, Chen Z, Miao Z, Yuan J, Wu Z (2023) Bi-functional biochar-g-C_3N_4-MgO composites for simultaneously minimizing pollution:photocatalytic degradation of pesticide and phosphorus recovery as slow-release fertilizer. J Environ Manage 344:118489. https://doi.org/10.1016/j.jenvman.2023.118489

Bahadoran A, Ramakrishna S, Masudy-Panah S, Roshan De Lile J, Sadeghi B, Li J, Gu J, Liu Q (2021) Novel S-scheme WO_3/CeO_2 heterojunction with enhanced photocatalytic degradation of sulfamerazine under visible light irradiation. Appl Surf Sci 568:150957. https://doi.org/10.1016/j.apsusc.2021.150957

Beizavi A, Boroujerdnia M (2024) Effect of g-C_3N_4 and rGO incorporation on the physical properties and photocatalytic application of TiO_2 particles through a simple and cost-effective synthesis method. Ceram Int 50:50317–50326. https://doi.org/10.1016/j.ceramint.2024.09.376

Bendahhou A, Yahakoub EH, Lemrini K, Moudrikah T, Raissi S, Lahrar EH, Malekshah RE, Chaou F, Jalafi I, Chourti K, El Miz M, El Barkany S, Abou-Salama M (2025) Photocatalytic degradation of methylene blue by tetragonal tungsten bronze modified by a heterojunction with graphitic-C_3N_4 in the presence of sunlight. J Alloys Compd 1020:179356. https://doi.org/10.1016/j.jallcom.2025.179356

Bian F, Wu X, Li S, Qin G, Meng X, Wang Y, Yang H (2021) Role of transport polarization in electrocatalysis: a case study of the Ni-cluster/graphene interface. J Mater Sci Technol 92:120–128. https://doi.org/10.1016/j.jmst.2021.03.035

Camacho-Munoz D, Lawton LA, Edwards C (2020) Degradation of okadaic acid in seawater by UV/TiO_2 photocatalysis - proof of concept. Sci Total Environ 733:139346. https://doi.org/10.1016/j.scitotenv.2020.139346

Chaudhuri P, Pande R, Baraiya NA (2025) From char to flame: evaluating bamboo bio-char combustion via cone calorimetry and thermogravimetric analysis. Energy 314:134313. https://doi.org/10.1016/j.energy.2024.134313

Chen C, Yang S, Ding J, Wang G, Zhong L, Zhao S, Zang Y, Jiang J, Ding L, Zhao Y, Liu L, Ren N (2021) Non-covalent self-assembly synthesis of AQ_2S@

rGO nanocomposite for the degradation of sulfadiazine under solar irradiation: the indispensable effect of chloride. Appl Catal B Environ 298:120495. https://doi.org/10.1016/j.apcatb.2021.120495

Cheng M, Li H, Wu Z, Yu Z, Tao X, Huang L (2025) Synergistic effects of CQDs and oxygen vacancies on CeO_2 photocatalyst for efficient photocatalytic nitrogen fixation. Sep Purif Technol 354:129299. https://doi.org/10.1016/j.seppur.2024.129299

Cui T, Zhang Y, Tian M, Yan Y, Zhang G, Zhang T, Zhao J, Jiang J (2024) Construction of TiO_2 on cotton straw deposited on g-C_3N_4 heterojunction to improve the photocatalytic degradation activity of methylene blue and tetracycline. Diamond Relat Mater 144:111028. https://doi.org/10.1016/j.diamond.2024.111028

Duan Y, Deng L, Shi Z, Liu X, Zeng H, Zhang H, Crittenden J (2020) Efficient sulfadiazine degradation via in-situ epitaxial grow of graphitic carbon nitride (g-C_3N_4) on carbon dots heterostructures under visible light irradiation: synthesis, mechanisms and toxicity evaluation. J Colloid Interface Sci 561:696–707. https://doi.org/10.1016/j.jcis.2019.11.046

Fazal T, Razzaq A, Javed F, Hafeez A, Rashid N, Amjad US, Ur Rehman MS, Faisal A, Rehman F (2020) Integrating adsorption and photocatalysis: a cost effective strategy for textile wastewater treatment using hybrid biochar-TiO_2 composite. J Hazard Mater 390:121623. https://doi.org/10.1016/j.jhazmat.2019.121623

Guo Q, Zhou C, Ma Z, Yang X (2019) Fundamentals of TiO_2 photocatalysis: concepts, mechanisms, and challenges. Adv Mater 31(50):e1901997. https://doi.org/10.1002/adma.201901997

Guo F, Chen J, Zhao J, Chen Z, Xia D, Zhan Z, Wang Q (2020) Z-scheme heterojunction g-C_3N_4@PDA/BiOBr with biomimetic polydopamine as electron transfer mediators for enhanced visible-light driven degradation of sulfamethoxazole. Chem Eng J 386:124014. https://doi.org/10.1016/j.cej.2020.124014

Hou N, Li X, Jiang X, Zhang N, Wang R, Li D (2022) The role of biochar in the photocatalytic treatment of a mixture of Cr (VI) and phenol pollutants: biochar as a carrier for transferring and storing electrons. Sci Total Environ 844:157145. https://doi.org/10.1016/j.scitotenv.2022.157145

Hu Z, Chen C, O Hare D, Lei J, Liu J (2025) Recent advances in photocatalysis of layered double hydroxide-biochar composites. ACS Mater Lett 7(8):2732–2748. https://doi.org/10.1021/acsmaterialslett.5C00673

Huang C, Lu G, Cheng Z, Jiang P, Cong R, Yang T (2025) Understanding the photocatalytic water reduction capability of NaM $(WO_4)_2$ (m=ga, sc) by the electronic structure and bond characteristic analysis. Inorg Chem. https://doi.org/10.1021/acs.inorgchem.5c00556

K C A, Rao CS, Nair V (2024) Combination of ensemble machine learning models in photocatalytic studies using nano TiO_2—lignin based biochar. Chemosphere 352:141326. https://doi.org/10.1016/j.chemosphere.2024.141326

Kahkeci J, Gamal El-Din M (2023) Biochar-supported photocatalysts: performance optimization and applications in emerging contaminant removal from wastewater. Chem Eng J 476:146530. https://doi.org/10.1016/j.cej.2023.146530

Kane A, Chafiq L, Dalhatou S, Bonnet P, Nasr M, Gaillard N, Dikdim JMD, Monier G, Assadi AA, Zeghioud H (2022) G-C_3N_4/TiO_2 s-scheme heterojunction photocatalyst with enhanced photocatalytic carbamazepine degradation and mineralization. J Photochem Photobiol Chem 430:113971. https://doi.org/10.1016/j.jphotochem.2022.113971

Klienchen De Maria VP, Guedes De Paiva FF, Tamashiro JR, Silva LHP, Da Silva Pinho G, Rubio-Marcos F, Kinoshita A (2024) Advances in ZnO nanoparticles in building material: antimicrobial and photocatalytic applications – systematic literature review. Constr Build Mater 417:135337. https://doi.org/10.1016/j.conbuildmat.2024.135337

Klüpfel L, Keiluweit M, Kleber M, Sander M (2014) Redox properties of plant biomass-derived black carbon (biochar). Environ Sci Technol 48(10):5601–5611. https://doi.org/10.1021/es500906d

Kuan J, Zhang H, Gu H, Zhang Y, Wu H, Mao N (2022) Adsorption-enhanced photocatalytic property of Ag-doped biochar/g-C_3N_4/TiO_2 composite by incorporating cotton-based biochar. Nanotechnology. https://doi.org/10.1088/1361-6528/ac705e

Li D, Li R, Zeng F, Yan W, Deng M, Cai S (2023) The photoexcited electron transfer and photocatalytic mechanism of g-C_3N_4/TiO_2 heterojunctions: time-domain *ab initio* analysis. Appl Surf Sci 614:156104. https://doi.org/10.1016/j.apsusc.2022.156104

Li C, Wu J, Wang X, Cai Y, Jia R, Wang W, Xia S, Li L, Chen Z, Jin C (2024a) One-step preparation of Z-scheme g-C_3N_4 nanorods/TiO_2 microsphere with improved photodegradation of antibiotic residue. Ceram Int 50(21):42127–42134. https://doi.org/10.1016/j.ceramint.2024.08.056

Li H, Cheng B, Xu J, Yu J, Cao S (2024b) Crystalline carbon nitrides for photocatalysis. EES Catalysis. https://doi.org/10.1039/d3ey00302g

Li T, Chen Y, Cheng Y, Zheng M, Qian J, He M, Chen Q, Zhang Z (2024c) Synthesis of rare earth MOF/CZS materials derived from aromatic tetracarboxylic acids and photocatalytic hydrogen production. Int J Hydrogen Energy 65:225–235. https://doi.org/10.1016/j.ijhydene.2024.04.043

Li Y, Liu C, Li Q, Mao S (2024d) Fluorescence analysis of antibiotics and antibiotic-resistance genes in the environment: a mini review. Chin Chem Lett 35(10):109541. https://doi.org/10.1016/j.cclet.2024.109541

Li Y, Wang Y, Yang H, Kong L, Dou M, Cui Y, Dou J (2024e) Modification of electron transfer paths in CdS-TiO_2 Z-type heterojunction by cobalt-based complexes for boosting visible-light photocatalytic hydrogen evolution. J Alloys Compd 1002:175324. https://doi.org/10.1016/j.jallcom.2024.175324

Li C, Zhang Y, Tian M, Ahmad N, Jia K, Luo Z, Qiao B, Cheng J, Zhao C (2025) Porphyrinic based hydrogen-bonded organic framework/TiO_2 nanocomposites for efficient photocatalytic degradation of sulfadiazine. J Environ Sci (China) 152:287–301. https://doi.org/10.1016/j.jes.2024.05.015

Liang L, Gao S, Zhu J, Wang L, Xiong Y, Xia X, Yang L (2020) The enhanced photocatalytic performance toward carbamazepine by nitrogen-doped carbon dots decorated on BiOBr/CeO_2: mechanism insight and degradation pathways. Chem Eng J 391:123599. https://doi.org/10.1016/j.cej.2019.123599

Lin Y, Wang Q, Ma M, Li P, Maheskumar V, Jiang Z, Zhang R (2021) Enhanced optical absorption and photocatalytic water splitting of g-C_3N_4/TiO_2 heterostructure through c&b codoping: a hybrid DFT study. Int J Hydrogen Energy 46(14):9417–9432. https://doi.org/10.1016/j.ijhydene.2020.12.114

Liu X, Liu Y, Lu S, Guo W, Xi B (2018) Performance and mechanism into TiO_2/zeolite composites for sulfadiazine adsorption and photodegradation. Chem Eng J 350:131–147. https://doi.org/10.1016/j.cej.2018.05.141

Liu G, Xu S, Li W, Wang Z, Cui J (2024a) Efficient visible light catalytic degradation of toxic organic pollution by hollow urchin-like TiO_2@g-C_3N_4/GQDs composite. Ceram Int 50(16):28064–28077. https://doi.org/10.1016/j.ceramint.2024.05.104

Liu J, Zou R, Zhang H, Song Y, Liu Y, Yang S, Xia R, Iwuoha EI, Feleni U, Admassie S, Peng X (2024b) Enhanced π-electron transport in graphitic carbon nitride (g-C_3N_4) by constructing biochar-welded donor-acceptor (D-A) configuration for photocatalytic conversion of biomass. Appl Catal Environ Energ 357:124312. https://doi.org/10.1016/j.apcatb.2024.124312

Liu H, Ciric L, Bhatti M (2025) Promotion mechanism of nanomaterials and modified/combined nanomaterials on photodegradation of organic pollutants: a review based on meta-analysis. J Environ Manage 391:126428. https://doi.org/10.1016/j.jenvman.2025.126428

Long Z, Li Q, Wei T, Zhang G, Ren Z (2020) Historical development and prospects of photocatalysts for pollutant removal in water. J Hazard Mater 395:122599. https://doi.org/10.1016/j.jhazmat.2020.122599

Lu L, Yu W, Wang Y, Zhang K, Zhu X, Zhang Y, Wu Y, Ullah H, Xiao X, Chen B (2020) Application of biochar-based materials in environmental remediation: from multi-level structures to specific devices. Biochar 2(1):1–31. https://doi.org/10.1007/s42773-020-00041-7

Luo Y, Wang Y, Hua F, Xue M, Xie X, Xie Y, Yu S, Zhang L, Yin Z, Xie C, Hong Z (2023a) Adsorption and photodegradation of reactive red 120 with nickel-iron-layered double hydroxide/biochar composites. J Hazard Mater 443(Pt B):130300. https://doi.org/10.1016/j.jhazmat.2022.130300

Luo Y, Zheng A, Li J, Han Y, Xue M, Zhang L, Yin Z, Xie C, Chen Z, Ji L, Hong Z, Xie X (2023b) Integrated adsorption and photodegradation of tetracycline by bismuth oxycarbonate/biochar nanocomposites. Chem Eng J 457:141228. https://doi.org/10.1016/j.cej.2022.141228

Ma Z, Zhang L, Ma X, Zhang Y, Shi F (2022) Design of Z-scheme g-C_3N_4/BC/$Bi_{25}FeO_{40}$ photocatalyst with unique electron transfer channels for efficient degradation of tetracycline hydrochloride waste. Chemosphere 289:133262. https://doi.org/10.1016/j.chemosphere.2021.133262

Mafa PJ, Malefane ME, Opoku F, Sacko A, Oladipo AO, Lebelo SL, Liu D, Gui J, Mamba BB, Kuvarega AT (2023) Experimental and theoretical confirmation of CeFeCu trimetal oxide/Bi_2O_3 S-scheme heterojunction for boosted photocatalytic degradation of sulfamethoxazole and toxicity evaluation. J Clean Prod 429:139519. https://doi.org/10.1016/j.jclepro.2023.139519

Meng Y, Huang Z, Liu D, Xie B, Guo Y, Xia S (2025) Enriched oxygen vacancies Bi_2WO_6-Ov@LDHs photoactivated persulfate degradation of tetracycline: synergistic effect of Z-scheme heterojunction and variable valence state. J Environ Chem Eng 13(2):115942. https://doi.org/10.1016/j.jece.2025.115942

Miri A, Shih Y, Chen W (2024) The highly efficient photodegradation of 4-bromophenol by TiO_2/g-C_3N_4 nano photocatalyst with LED visible light. Chemosphere (Oxford) 362:142658. https://doi.org/10.1016/j.chemosphere.2024.142658

Orellana W (2021) D-π-a dye attached on TiO_2 (101) and TiO_2 (001) surfaces: electron transfer properties from ab initio calculations. Sol Energy 216:266–273. https://doi.org/10.1016/j.solener.2020.12.061

Othman Alqahtani F (2024) Advancing photocatalytic degradation under visible light with TiO_2/g-C_3N_4 nanohybrid mechanistic insights. J Saudi Chem Soc 28(5):101918. https://doi.org/10.1016/j.jscs.2024.101918

Paiman SH, Md Noor SF, Ngadi N, Nordin AH, Abdullah N (2023) Insight into photocatalysis technology as a promising approach to tackle microplastics pollution through degradation and upcycling. Chem Eng J 467:143534. https://doi.org/10.1016/j.cej.2023.143534

Pan H, Sun M, Wang X, Zhang M, Murugananthan M, Zhang Y (2022) A novel electric-assisted photocatalytic technique using self-doped TiO_2 nanotube films. Appl Catal B Environ 307:121174. https://doi.org/10.1016/j.apcatb.2022.121174

Paul DR, Sharma R, Nehra SP, Sharma A (2019) Effect of calcination temperature, ph and catalyst loading on photodegradation efficiency of urea derived graphitic carbon nitride towards methylene blue dye solution. RSC Adv 9(27):15381–15391. https://doi.org/10.1039/c9ra02201e

Qingge F, Huidong C, Haiying L, Siying Q, Zheng L, Dachao M, Yuyang Y (2018) Synthesis and structural characteristics of high surface area TiO_2 aerogels by ultrasonic-assisted sol–gel method. Nanotechnology 29(7):75702. https://doi.org/10.1088/1361-6528/aaa1d1

Rather RA, Singh S, Pal B (2017) A C_3N_4 surface passivated highly photoactive Au-TiO_2 tubular nanostructure for the efficient H_2 production from water under sunlight irradiation. Appl Catal B Environ 213:9–17. https://doi.org/10.1016/j.apcatb.2017.05.002

Sharmin F, Roy DC, Basith MA (2021) Photocatalytic water splitting ability of Fe/MgO-rGO nanocomposites towards hydrogen evolution. Int J Hydrogen Energy. https://doi.org/10.1016/j.ijhydene.2021.09.072

Shi Y, Lei X, Xia L, Wu Q, Yao W (2020) Enhanced photocatalytic hydrogen production activity of CdS coated with Zn-anchored carbon layer. Chem Eng J 393:124751. https://doi.org/10.1016/j.cej.2020.124751

Shi Q, Fang K, Chen W, Tan Y, Zhang C (2024) Designing a superhydrophobic cotton fiber coating exploiting TiO_2@g-C_3N_4 layered structure for augmented photocatalysis and efficient water-oil separation. Int J Biol Macromol 264:130596. https://doi.org/10.1016/j.ijbiomac.2024.130596

Song J, Zhang S, Li G, Du Q, Yang F (2020) Preparation of montmorillonite modified biochar with various temperatures and their mechanism for Zn ion removal. J Hazard Mater 391:121692. https://doi.org/10.1016/j.jhazmat.2019.121692

Su X, Wang X, Ge Z, Bao Z, Lin L, Chen Y, Dai W, Sun Y, Yuan H, Yang W, Meng J, Wang H, Pillai SC (2024) KOH-activated biochar and chitosan composites for efficient adsorption of industrial dye pollutants. Chem Eng J (1996) 486:150387. https://doi.org/10.1016/j.cej.2024.150387

Sun H, Liu J, Zhang C, Yuan Q, Ye Y, Yan W, Tian Z, Liang C (2019) S,N dual-doped carbon nanotubes as substrate to enhance the methanol oxidation performance of NiO nanoparticles. Carbon 152:114–119. https://doi.org/10.1016/j.carbon.2019.06.007

Sun S, Yao H, Fu W, Xue S, Zhang W (2020) Enhanced degradation of antibiotics by photo-fenton reactive membrane filtration. J Hazard Mater 386:121955. https://doi.org/10.1016/j.jhazmat.2019.121955

Tan Y, Li C, Sun Z, Liang C, Zheng S (2020) Ternary structural assembly of BiOCl/TiO_2/clinoptilolite composite: study of coupled mechanism and photocatalytic performance. J Colloid Interface Sci 564:143–154. https://doi.org/10.1016/j.jcis.2019.12.116

Tan Y, Shu R, Xu H, Song L, Zhang R, Ouyang C, Xia M, Hou J, Zhang X, Yuan Y, Zhang R (2023) Supercritical carbon dioxide-assisted TiO_2/g-C_3N_4 heterostructures tuning for efficient interfacial charge transfer and formaldehyde photo-degradation. J Environ Chem Eng 11(5):110992. https://doi.org/10.1016/j.jece.2023.110992

Thi Le T, Thi Le T, Tran Huu H, Thi To Nu D, Nguyen Thi L, Trang Phan TT, Nguyen VT, Nguyen Van K, Nguyen Phi H, Nguyen LT, Vo V (2024) Designing S-scheme of TiO_2@g-C_3N_4/graphene heterojunction with enhanced photocatalytic activity under visible light: experiments and DFT calculations. J Alloys Compd 995:174716. https://doi.org/10.1016/j.jallcom.2024.174716

Wang P, Guo X, Rao L, Wang C, Guo Y, Zhang L (2018) A weak-light-responsive TiO_2/g-C_3N_4 composite film: photocatalytic activity under low-intensity light irradiation. Environ Sci Pollut Res Int 25(20):20206–20216. https://doi.org/10.1007/s11356-018-2201-1

Wang J, Wang G, Wang X, Wu Y, Su Y, Tang H (2019) 3D/2D direct Z-scheme heterojunctions of hierarchical TiO_2 microflowers/g-C_3N_4 nanosheets with enhanced charge carrier separation for photocatalytic h_2 evolution. Carbon 149:618–626. https://doi.org/10.1016/j.carbon.2019.04.088

Wang J, Wang G, Cheng B, Yu J, Fan J (2021) Sulfur-doped g-C_3N_4/TiO_2 S-scheme heterojunction photocatalyst for congo red photodegradation. Chin J Catal 42(1):56–68. https://doi.org/10.1016/S1872-2067(20)63634-8

Wang G, Li Y, Dai J, Deng N (2022) Highly efficient photocatalytic oxidation of antibiotic ciprofloxacin using TiO_2@g-C_3N_4@biochar composite. Environ Sci Pollut Res Int 29(32):48522–48538. https://doi.org/10.1007/s11356-022-19269-w

Wang H, Wang S, Li J, Zhi S, Liu Y, Jiang K, Yang C, Wu D (2025a) A tale of two boron sites in g-C_3N_4: pulse laser-assisted modification and enhanced $2e^-$ preferences for photocatalytic H_2O_2 production. Chem Eng J (1996) 510:161862. https://doi.org/10.1016/j.cej.2025.161862

Wang R, Yin Z, Han X, Zhang Y, Zhang S, Lan X, Chen Y, Hong Z, Xie C, Xu J, Xue M (2025b) Ultra-durable ZIF-7 superhydrophobic coating for long-term corrosion protection in aircraft nacelles lips. Chem Eng J (1996) 518:164644. https://doi.org/10.1016/j.cej.2025.164644

Wei Y, Wang J, Ma J, Kong F, Xue J, Ye Z, Ma S, Zhao S (2024) Fabrication of porous biochar supported Bi_2MoO_6 photocatalyst for efficient degradation of ciprofloxacin in seawater under visible light irradiation: mechanistic investigation and intermediates analysis. Sep Purif Technol 349:127860. https://doi.org/10.1016/j.seppur.2024.127860

Winayu BNR, Liu Y, Chu H (2024) Competent visible light driven photocatalytic removal of gaseous styrene over TiO_2/g-C_3N_4 : characterization, parameters, kinetics, mechanism. J Taiwan Inst Chem Eng 164:105677. https://doi.org/10.1016/j.jtice.2024.105677

Wu Q, Song Y (2023) Enhanced interfacial charge migration through fabrication of p-n junction in $ZnIn_2S_4$/$NiFe_2O_4$/biochar composite for photocatalytic doxycycline hydrochloride degradation. Chem Eng J (1996) 453:139745. https://doi.org/10.1016/j.cej.2022.139745

Wu R, Yi J, Bao R, Liu P (2022) The excellent photocatalytic capability of TiO_2@C/O-doped g-C_3N_4 heterojunction photocatalyst. Colloids Surf A Physicochem Eng Asp 648:129351. https://doi.org/10.1016/j.colsurfa.2022.129351

Xiang X, Wu L, Zhu J, Li J, Liao X, Huang H, Fan J, Lv K (2021) Photocatalytic degradation of sulfadiazine in suspensions of TiO_2 nanosheets with exposed (001) facets. Chin Chem Lett 32(10):3215–3220. https://doi.org/10.1016/j.cclet.2021.03.064

Xu X, Meng L, Dai Y, Zhang M, Sun C, Yang S, He H, Wang S, Li H (2020) Bi spheres SPR-coupled Cu_2O/Bi_2MoO_6 with hollow spheres forming Z-scheme Cu_2O/Bi/Bi_2MoO_6 heterostructure for simultaneous photocatalytic decontamination of sulfadiazine and Ni (II). J Hazard Mater 381:120953. https://doi.org/10.1016/j.jhazmat.2019.120953

Xue W, Shi X, Guo J, Wen S, Lin W, He Q, Gao Y, Wang R, Xu Y (2024) Affecting factors and mechanism of removing antibiotics and antibiotic resistance genes by nano zero-valent iron (nZVI) and modified nZVI: a critical review. Water Res 253:121309. https://doi.org/10.1016/j.watres.2024.121309

Yousefzadeh F, Ghanbari M, Salavati-Niasari M (2023) Sonochemical synthesis and characterization of Sm_2CuO_4 nanostructures and their application as visible-light photocatalyst for degradation of water-soluble organic pollutants. Chemosphere 338:139564. https://doi.org/10.1016/j.chemosphere.2023.139564

Zahid M, Khan ZUH, Sun J, Muhammad N, Sabahat S, Shah NS, Iqbal J (2025) Biochar-derived photocatalysts for pharmaceutical waste removal, a sustainable approach to water purification. Appl Surf Sci Adv 26:100721. https://doi.org/10.1016/j.apsadv.2025.100721

Zang Y, Yang S, Chen C, Liu J, Ding L, Pang J, Wu C, Liu P, Zhang L, Ren N, Ding J (2024) Simulated solar light-driven degradation of micropollutant in water by biochar-based metal-free catalyst: regulation strategies for electronic structure and morphology engineering. Chem Eng J 488:151062. https://doi.org/10.1016/j.cej.2024.151062

Zeng L, Ding X, Sun Z, Hua W, Song W, Liu S, Huang L (2018) Enhancement of photocatalytic hydrogen evolution activity of g-C_3N_4 induced by structural distortion via post-fluorination treatment. Appl Catal B-Environ 227:276–284. https://doi.org/10.1016/j.apcatb.2018.01.040

Zhang Y, Ren X, Yang L, Chen Z (2021) Z-scheme TiO_2/g-C_3N_4 composites prepared by hydrothermal assisted thermal polymerization with enhanced visible light photocatalytic activity. Res Chem Intermed 47:1503–1518. https://doi.org/10.1007/s11164-020-04379-2

Zhang S, Zhi S, Wang H, Guo J, Sun W, Zhang L, Jiang Y, Zhang X, Jiang K, Wu D (2022) Laser-assisted rapid synthesis of anatase/rutile TiO2 heterojunction with function-speciffed micro-zones for the effective photo-oxidation of sulfamethoxazole. Chem Eng J 453:1139702. https://doi.org/10.1016/j.cej.2022.139702

Zhang H, Bian H, Wang F, Zhu L, Zhang S, Xia D (2023a) Enhanced photocatalytic reduction of CO_2 over pg-C_3N_4-supported TiO_2 nanoparticles with ag modification. Coll Surfac Physicochem Engin Asp 674:131989. https://doi.org/10.1016/j.colsurfa.2023.131989

Zhang H, Liu Y, Liu N, Kang S (2023b) Understanding the interface properties of photocatalytic reactors for rational engineering applications. Chem Eng J 472:145057. https://doi.org/10.1016/j.cej.2023.145057

Zhang Y, Li Y, Yuan Y (2023c) Enhanced sulfamethoxazole photodegradation by N-$SrTiO_3$/$NH_4V_4O_{10}$ S-scheme photocatalyst: DFT calculation and photocatalytic mechanism insight. J Colloid Interface Sci 645:860–869. https://doi.org/10.1016/j.jcis.2023.05.037

Zheng C, Guo Y, Zhang C, Cao X, Wan J (2025) Nitrogen-defective protonated porous C_3N_4 nanosheets for enhanced photocatalytic hydrogen production under visible light. Appl Catal B 365:124879. https://doi.org/10.1016/j.apcatb.2024.124879

Zhou L, Wang L, Lei J, Liu Y, Zhang J (2017) Fabrication of TiO_2/Co-g-C_3N_4 heterojunction catalyst and its photocatalytic performance. Catal Commun 89:125–128. https://doi.org/10.1016/j.catcom.2016.09.022

Zhou X, Xian Y, Li Z, Yujie C, Luo J, Ning X, Fan X, Zhong Y, Zhou X (2025) All-solid-state red phosphorus/RGO/WO_3 Z-scheme heterostructure for photocatalytic overall water splitting. Sep Purif Technol 357:130117. https://doi.org/10.1016/j.seppur.2024.130117

Zhu J, Zhu Y, Chen Z, Zhao Y, Chen G (2024) Fluorine-doped TiO_2/SiO_2/activated carbon ternary hybrids: enhancing adsorption and photocatalytic degradation of rhodamine b and methyl orange. Mater Res Bull 176:112826. https://doi.org/10.1016/j.materresbull.2024.112826

Zhu H, Zhang Y, Jia Y, Cheng D, Feng Y, Duan L (2025) Efficient photocatalyst for overall water-splitting hydrogen generation using a direct Z-scheme $MoTe_2$/SnS_2 van der waals heterostructure. Micro Nanostruct 207:208270. https://doi.org/10.1016/j.micrna.2025.208270